This is a repository copy of *Microtopography of bare peat: a conceptual model and objective classification from high-resolution topographic survey data*.

White Rose Research Online URL for this paper:
http://eprints.whiterose.ac.uk/125891/

Version: Accepted Version

Article:

Microtopography of bare peat: a conceptual model and objective classification from high-resolution topographic survey data

Smith, M.W.[1]* and Warburton, J.[2]

[1] water@Leeds, School of Geography, University of Leeds, Woodhouse Lane, Leeds, LS2 9JT, UK.

[2] Department of Geography, Durham University, Lower Mountjoy, South Road, Durham, DH1 3LE, UK.

*Corresponding author: m.w.smith@leeds.ac.uk +44(0)113 3431974

Abstract

Peatlands globally are at risk of degradation through increased susceptibility to erosion as a result of climate change. Quantification of peat erosion and an understanding of the processes responsible for their degradation is required if eroded peatlands are to be protected and restored. Owing to the unique material properties of peat, fine-scale microtopographic expressions of surface processes are especially pronounced and present a potentially rich source of geomorphological information, providing valuable insights into the stability and dominant surface process regimes. We present a new process-form conceptual framework to rigorously describe bare peat microtopography and use Structure-from-Motion (SfM) surveys to quantify roughness for different peat surfaces. Through the first geomorphological application of a survey-grade structured-light hand-held 3D imager (HhI), which can represent sub-millimetre topographic variability in field conditions, we demonstrate that SfM identifies roughness signatures reliably over bare peat plots (<1 m^2), although some smoothing is observed. Across 55 plots, the roughness of microtopographic types is quantified using a suite of roughness metrics and an objective classification system derived

from decision tree analysis with 98% success. This objective classification requires just five roughness metrics, each of which quantifies a different aspect of the surface morphology. We show that through a combination of roughness metrics, microtopographic types can be identified objectively from high resolution survey data, providing a much-needed geomorphological process-perspective to observations of eroded peat volumes and earth surface change.

Keywords: peat; microtopography; Structure-from-Motion; structured-light imager; roughness

1. Introduction

Globally, peatlands contain 30−50% of all carbon stored in soils (Gorham, 1991) much of which is at risk of degradation through climate change (Gallego-Sala and Prentice, 2012), increasing its susceptibility to erosion. Once vegetation is removed, bare peat surfaces can be subject to accelerated erosion, the rate of which is determined by the dominant agent of erosion. Bare upland peat is particularly subject to erosion by water, wind and frost, alongside chemical oxidation (peat wastage) (Evans and Warburton, 2007). Thus, there is an urgent need to understand erosion drivers and ways of building resilience into human-disturbed peatland systems. Yet, existing geomorphological data is very sparse.

Blanket peat covers 7.5% of the British Isles (Tallis et al., 1997) where there has been widespread erosion and large carbon losses exacerbated by human interventions over the past century (Evans and Warburton, 2007). Erosion by flowing water is the dominant component in most UK peatlands; but local topography exerts a strong control in determining process dominance (Evans and Warburton, 2007). This has yet to be quantified accurately. Bare peat surface microtopography is especially dynamic and patchy; different surface

processes leave distinctive topographic roughness signatures and local surface microtopography can adjust rapidly in response to changing processes over relatively short timescales (Foulds and Warburton, 2007). For example, rainsplash leaves a pitted surface while surface wash results in linear grooves distinguished from wind-formed features due to their orientation (Evans and Warburton, 2007). Areas of peat deposition are smoother, while processes that increase sediment supply (freeze-thaw, desiccation) result in highly fragmented surfaces of small-scale roughness and aggregates (Repo et al., 2006). Roughness varies subtly with dominant process and can be classified according to process regimes (Bower, 1959; Evans and Warburton, 2007). The microtopography which results has a major impact on local water tables (Charman, 2002), surface aerodynamic roughness (Warburton 2003), overland flow hydraulics (Dunkerley, 2002), aeration (oxidation) of the acrotelm surface layer (Birnie, 1993) and gaseous emissions (Repo et al., 2009).

Quantification of peat erosion has traditionally relied on sediment budgets extrapolated from local point-based direct measurements of erosion and deposition (e.g. erosion pins) (Evans and Warburton, 2005; Evans et al., 2006). While such measurements provide valuable information on peatland dynamics, they are limited in terms of process understanding by the paucity of specific process measurements and inherent spatial and temporal averaging (Warburton, 2003). High-resolution topographic survey techniques can be applied to partly address these limitations. Airborne LiDAR (or ALS) provides high-resolution (~m) topography with decimetre accuracy at landscape scales. In peatlands ALS has been used to explore the topographic context of gully erosion (Evans and Lindsay, 2010); however, gully erosion is only one component of peat erosion. Small-scale erosion features cannot be detected and the contribution of other peat surface processes such as surface wash, rainsplash and wind erosion to total erosion volumes remains unclear.

High resolution topographic survey data can quantify sediment losses from peatlands and thereby evaluate the effectiveness of peatland restoration schemes (e.g. to feed into the UK

Peatland Code; IUCN UK Peatland Programme, 2017). Similar methods are now relatively commonplace throughout geomorphology (Williams, 2012). However, high resolution data sets contain a wealth of hitherto untapped information on surface properties that can help elucidate not just the extent of topographic change, but also infer the process through which these changes occurred by quantifying and examining topographic roughness signatures (Smith, 2014). The roughness of bare peat surfaces is important because surface roughness has feedbacks with near-surface sediment transfer mechanisms (Evans and Warburton, 2005) while the relative magnitude and direction of the sediment transfer process can be inferred from close inspection of the surface roughness at small scales. Peatlands represent an ideal case study of such an approach, since the low dry density of peat (~0.1 t m^{-3}) means that volumetric removal of peat is ~15 times greater than that represented by an equivalent dry mass of mineral material (Evans and Warburton, 2007). This property renders peat more susceptible to entrainment and transport; consequently, a wide range of surface features have been observed representing a range of processes. Moreover, it also means that these systems, being more susceptible to large volumetric changes, are ideal for the construction of morphometric sediment budgets. If peat microtopographic-types can be identified objectively from topographic data sets, this opens up a wealth of new information to inform geomorphological process interpretations.

Recent work has identified the potential of terrestrial laser scanning (TLS) to represent fine-scale topographic variability of peatlands (Anderson et al., 2010; Luscombe et al., 2015) and to quantify erosion and deposition in peatlands (Grayson et al., 2012) through the construction of morphometric sediment budgets. In addition, Structure-from-Motion (SfM) has emerged as a potential alternative (Mercer and Westbrook, 2016) and has been used extensively to quantify the microtopography and erosion of soil surfaces (e.g. Castillo et al., 2012; Ouédraogo et al., 2014; Nouwakpo et al., 2014; Bauer et al., 2015; Kaiser et al., 2015). SfM, typically coupled with Multi-View Stereo (MVS) algorithms, generates point clouds from aerial or oblique imagery using consumer-grade digital cameras, without the

need for expensive hardware (James and Robson, 2012; Westoby et al., 2012; Fonstad et al., 2013; Smith et al., 2015). SfM-MVS data are typically less precise than obtained with TLS though this depends on survey range. A recent synthesis of 50 SfM surveys in geomorphology by Smith and Vericat (2015) demonstrated the dependence of SfM-MVS accuracy (root-mean squared error, RMSE) on survey range, observing a ratio of 1:639 (though James et al. (2017) suggest that this can be improved to 1:1000 with more robust photogrammetric workflows). Thus, SfM from 150 m altitude imagery is of similar accuracy to ALS and is potentially better than TLS from short ranges using ground-based imagery (Smith and Vericat, 2015). However, validating the capabilities of SfM-MVS at short ranges in the field is problematic owing to the lack of superior reference data (Eltner et al., 2016).

Most recently, portable 3D hand-held imagers (HhI) have become available that use a single-frame coding method from structured light imaging. They are typically used in surface metrology to test the quality of finished manufactured surfaces, as part of forensic crime scene investigations and in the construction industry to survey areas with limited access (OR3D, 2015). The mobility, ruggedness and versatility of HhIs renders them ideal for peatland geomorphology. While other researchers have adapted the similar and more affordable (~£100) Microsoft® Kinect™ sensor for geomorphological data collection (e.g. Mankoff and Russo, 2013; Hämmerle et al., 2014; Chávez et al., 2014; Tortini et al., 2014; Thomsen et al., 2015; Nicholson et al. 2016), the Kinect™ was initially designed to detect human motion in an indoor environment and is not best suited to use in the field, being readily saturated by sunlight in an outdoor setting (Chávez et al., 2014).

The overall aims of this study are (i) to establish an objective and reproducible classification of bare peat surface microtopography from high resolution topographic data; and (ii) to test whether close-range SfM-MVS can provide topographic data of sufficient precision to allow this classification to be used in practice. To address these aims, we present three objectives:

(1) To outline a new conceptual framework of peat surface roughness types by relating observed forms to the dominant processes responsible for their formation;

(2) To establish whether SfM-MVS can meaningfully reproduce millimetre-scale roughness metrics that can be used to examine topographic roughness signatures of peat surfaces through validation against HhI data; and

(3) To objectively define a typology of peat roughness based on plot-scale (<1 m^2) SfM-MVS surveys and a range of roughness metrics.

2. Conceptual framework of peat surface roughness

Bare peat is highly responsive to changing environmental forces acting at the near surface and characteristic microtopographies emerge in response to rainfall, surface wash, wind action and fluctuations in surface temperature (both heating (drying, desiccation) and freezing) (Bower, 1959; Evans and Warburton, 2007) (Figure 1). Bower (1959) was one of the first observers to recognise that the detailed surface features of bare peat retain evidence in their microtopography of relative importance of the interaction between material properties and the main agents of surface erosion. Therefore spatial and temporal variations in surface roughness reflect contrasts in the physical properties of the peat and key erosion processes acting in combination (Evans and Warburton, 2007).

[FIGURE 1]

In terms of the processes which generate small scale irregularities of the peat surface, the direct impact of rainfall, surface wash, wind action and changes in surface temperature (freezing and drying) are recognised as the key natural drivers in conditioning bare peat roughness (Evans and Warburton, 2007). Figure 2 provides a conceptual model of process-form linkages of bare peat surfaces. The diagram is a matrix showing the relationships between the four key surface processes and the typical surface roughness characteristics resulting from these interactions. The framework proposed in Figure 2 provides a

comprehensive assessment of the 'natural' processes operating on bare upland peat surfaces and is designed to capture the key process-form relationships caused by wind, rain and temperature variations acting on bare peat surfaces. Each of the panels in the matrix represents a schematic showing the typical two dimensional (cross-section) form and scale of the surface roughness. Each panel shows a length scale of 1 m and a vertical scale of 0.1 m. Generally the scale of the observed roughness will increase with intensity of process, e.g. roughness increases along a trajectory from the bottom-left to top-right in each of the panels. The 1 m length scale is significant because for the purposes of this paper bare peat surface microtopography is operationally defined as small-scale surface features whose repeated structures are recognised at scales of < 1 m. The scale of these features is therefore generally smaller than the typical microforms (e.g. mounds, haggs, and ridges) included in the ecological classification of mires (Lindsay, 1995; Warburton, 2003) but generally larger than the engineering classification of peat structure which is based on texture and macrofossil content (Radforth, 1969). In the square matrix shown in Figure 2, examples of surface roughness types associated with the four panels of the leading diagonal are also shown in Figure 1 for comparison with the schematic.

[FIGURE 2]

The physical basis for this framework is well-established from decades of field observations (Bower, 1959; Bower, 1961; Warburton, 2003; Evans and Warburton, 2007; Foulds and Warburton, 2007) but this is the first time this has been brought together in terms of a process-form conceptual model. Peatland scientists have had a long-term interest in surface microtopography but this has mostly concentrated on vegetated surfaces (Pearsall, 1956; Lindsay et al., 1985; Pellerin et al., 2006). Bare peat surfaces have not been systematically described. The conceptual framework shows the typical roughness types associated with the key process regimes, shown in the panels of the leading diagonal. Rainfall results in a pitted surface whose roughness increases with intensity resulting in a typical toothed surface of

raised **pedestals** (Figure 1a) (Bower, 1959). If this occurs in association with surface wash and/or wind-driven rain then there is a directional flux of eroded peat which leads to the development of asymmetrical roughness aligned in the direction of the prevailing wind or local slope (Warburton, 2003). If the flux is high enough then small **microterraces** or benches (vertical relief c. 0.1 m) can develop (Figure 1f) (Evans and Warburton, 2007). Surface wash will tend to transport eroded peat along hydraulic gradients ponding in surface depressions, infilling the local microtopography and generally producing a smooth surface (Figure 1b). If this occurs in association with wind, microterraces can develop whose upper surfaces are smoothed by the wash process forming small **peat flats** (Hulme and Blyth, 1985; Warburton, 2003).

Prolonged exposure of bare peat surfaces to wind results in surface desiccation and the development of a surface crust (Foulds and Warburton, 2007) (Figure 1c). With increased duration the crust may be locally entrained and rolled over producing ridges of dry peat projecting up to 0.1 m above the general surface. Under wet conditions and high wind-driven sediment flux features akin to climbing ripples are observed and these leave distinct small-scale **wind ridges** (Figure 1e) (Evans and Warburton, 2007). Changes in temperature also have an important impact on surface roughness. Both prolonged warm temperatures (local drought) and cold winter temperatures (surface freezing) can lead to surface desiccation resulting initially in small scale cracking which with prolonged duration can result in large desiccation cracks exceeding several decimetres in depth (Figure 1d) (Francis, 1990). In the presence of moisture (under rain and surface wash conditions) freezing temperatures can result in local frost heave which breaks up the surface and produces frost-fluff or nubbins (Washburn, 1979; Repo et al., 2006). Therefore it can be seen that there is a clear link between the dominant process regimes acting on a bare peat surface and the characteristic types of roughness which evolve. Although some equifinality is evident in the resultant microtopography (e.g. surface wash and wind-driven rain), subtleties in the roughness can

be used to differentiate the dominant processes which have acted to produce the characteristic roughness forms.

The framework proposed in Figure 2 applies to 'natural' processes operating on bare upland peat surfaces and is based on past research and direct observations of surfaces over multiple years (Evans and Warburton, 2007). It provides a clear framework for generating hypotheses that can be tested by quantitative measurements and usefully identifies examples where different processes result in similarity of form (equifinality). The classification in Figure 2 can be extended to include other processes such as peat mining (Campbell et al., 2002; Tuukkanen et al., 2014), animal trampling (Pellerin et al., 2006) and burning (Maltby et al., 1990) which also act to influence surface roughness; but in this initial test our assessment is deliberately restricted to include the dominant natural processes acting on peat surfaces.

3. Methods and Study Site

3.1 Study Site

The study area is located in the Moor House–Upper Teesdale National Nature Reserve in the North Pennine uplands in Northern England (Figure 3). The bedrock geology is part of the Carboniferous series composed of interbedded sandstone, shale and limestone which is overlain by periglacial deposits of reworked till and overbank deposits. The clay-rich nature of the basal sediments allows development of blanket peat even on limestone bedrock. Ombrotrophic blanket peat is the dominant soil type and varies in depth from 1 to 3 m, but can locally exceed 9 m. It is estimated that approximately 17% of the blanket peat cover is eroded (Garnett and Adamson, 1997), with dendritic gullying dominating on lower angled slopes and linear gullying on the steeper slopes (Bower, 1961).

On flatter ground areas of bare peat occur and the study site, Moss Flats, is a 0.5 ha area of bare peat (2014 estimate) which forms a significant erosional subsystem of the Rough Sike catchment (Figure 3). Average erosion rates are 0.47 t ha a^{-1} (Warburton, 2003). The bare peat surface (Figures 1 and 3) consists of a mosaic of flats, terraces, pedestals, wind ridges and haggs representing an assemblage of typical erosional and deposition forms associated with an active area of upland bare peat. The climate is 'Upland Maritime' being characterized by cool, cloudy and wet conditions (Manley, 1942, 1943; Smithson, 1985). High winds are common and annual precipitation is approximately 2000 mm. The prevailing wind direction is from the southwest. In winter ground surface freezing occurs in the upper few centimetres of the peat and during summer periods of reduced rainfall, short periods of drought result in surface desiccation of the peat (Foulds and Warburton, 2007). Surveys took place in April 2016 on a mild day with no rainfall. As such, some roughness types were not exhibited (e.g. desiccation cracking, frost fluff).

[FIGURE 3]

3.2 Structure from Motion Multi-View Stereo (SfM-MVS) Surveys

To characterize the millimetre-scale variability of peat surface microtopography, 55 bare peat plots were surveyed using Structure-from-Motion with Multi-View Stereo (SfM-MVS) photogrammetric techniques, following the guidance outlined in Smith et al. (2015) and detailed below. Plots were between 0.5 and 0.9 m^2 and were typically surveyed in groups of four within a single SfM-MVS survey. Using a Panasonic DMC-TZ60 camera (focal length 4 mm which is a 35-mm focal length equivalent of 25 mm), oblique convergent 18 Megapixel images were taken from viewpoints surrounding the plots that were ~1.5 m above ground to mitigate against the doming effect as described in James and Robson (2014). Approximately 34 images were taken for each survey and angular changes of < 20° between adjacent camera locations were ensured to facilitate correct identification and matching of keypoints

(Moreels and Peronas, 2007; Bemis et al., 2014). The resulting ground pixel size was sub-mm (~0.7 mm). Plots were distributed over Moss Flats to incorporate the greatest possible range of surface roughness types and topographic variability and to provide good spatial coverage across the bare peat area (Figure 3). The clustering of plots in groups of around four permitted the evaluation of both the inherent variability in the microtopography (at a single location) and larger-scale effects of aspect, topographic position and exposure to the wind (i.e. to check that the results were consistent across the site for a given microtopographic type). Plots were classified according to their microtopography into a four-fold classification system based upon the scheme outlined in Section 2: peat flats (14 plots), pedestals (8 plots), wind ridges (20 plots) and microterraces (13 plots). Note that not all of the microtopographic types outlined in Section 2 were identified at the site during the April 2016 surveys as several roughness types are only emergent following particular environmental conditions.

Photographs were imported into Agisoft Photoscan Professional 1.2.5 and SfM algorithms implemented, estimating simultaneously camera positions, camera intrinsic parameters and scene geometry. See James and Robson (2012) and Smith et al. (2015) for further details. Georeferencing was performed using 5 survey disc targets of 50 mm diameter surrounding each survey area that were surveyed using a Leica TS15i reflectorless total station (TPS). Three-dimensional co-ordinates were recorded in a local co-ordinate system. Averaging ten readings for each target yielded a sub-mm precision in TPS co-ordinates. Survey disc targets were identified in the imagery and the 3D co-ordinates from the total station survey were then imported and a linear similarity transformation performed to scale and georeference each SfM point cloud. Georeferencing errors were all sub-cm, with the majority of surveys <4 mm and identified to within ~3 pixels. MVS image matching algorithms were performed to produce final dense point clouds with an average point density of ~1.4 Mn points m^{-2} (i.e. 1.4 points mm^{-2}). Point clouds were then imported into CloudCompare

(Girardeau-Montaut, 2016) and plots were linearly detrended and normal vectors of each point computed.

Since some roughness metrics are calculated using a Digital Elevation Model (DEM) while others are calculated using the point cloud directly, two output topographic data products were required for roughness analysis (section 3.4):

(1) A 5 mm resolution DEM was generated using the mean point elevation in each cell (following Mercer and Westbrook, 2016);

(2) A sub-sampled point cloud was generated through octree subsampling (level 7), a data decimation step that reduces the point density, ensures a more uniform point distribution in 3D space where data are available (octree cell size was typically 7 mm) and prevents clusters of points from influencing the results.

Neither DEMs nor point clouds were interpolated. For the three plots used to evaluate SfM against the HhI, an additional 1 mm resolution DEM was generated using the mean elevation observed in each cell to examine the limits of the SfM data, though the 5 mm DEMs were used for roughness analysis.

3.3 Hand-Held Imager

Three plots comprising a range of roughness types were also surveyed using a Mantis Vision F5 Short-Range 3D Imager to provide a reference topographic data set. Since, to the authors' knowledge, this study represents the first use of a survey-grade hand held 3D imaging system in geomorphology, the instrument will be described in detail.

The Mantis Vision F5-Short Range Hand-held 3D Imager (hereafter referred to as a Hand-held Imager or HhI) operates using near infrared structured light technology similar to the aforementioned Kinect[TM] sensor. Near infrared light is projected through a mask containing a

proprietary single-coded-light pattern. This pattern is projected onto a 3D surface in a single instantaneous snapshot. The deformation pattern is then sensed by the instrument and using index information in the structured light, active triangulation algorithms can determine a full 3D image. The nature of the codification method permits a point density of ~50,000 points per frame that is an order of magnitude greater than alternative systems. With a rate of 10 frames-per-second, the HhI is thus capable of acquiring 0.5 Mn points per second (OR3D, 2015). The data is then downloaded into Mantis Vision's 3D production software where each frame is converted into a dense point-cloud. Owing to the short time interval between frames (0.1 s) each frame is then registered with the previous to create a final dense model and an automatic global alignment process reduces any misalignment during the cloud registration process. The point spacing of a single frame is ~1.6 mm (at 0.5 m range) though since the 3D surface is derived from a composite of multiple frames, the final point density is unlimited. The stated 3D point accuracy of the F5-SR is 0.05 mm, though trials suggest such accuracies are not always achievable (Kersten et al., 2016). The system compares favourably with the maximum point accuracy of the Kinect ^{TM} (~1 mm; Tortini et al., 2014) which Lachat et al. (2015) found to be challenging for accurate 3D modelling even in an indoor setting.

The HhI hardware consists of a video camera and a projector, both of which are integrated into a grab handle (Figure 4). It is ideally suited to small-scale geomorphological investigation as it weighs just 0.6 kg, is rugged for use in an outdoor environment and can be used in a wide range of lighting conditions (from complete darkness to direct sunlight as it is resistant to sun flashes). The operating range is 0.3 – 0.8 m with a maximum field of view of 0.55 x 0.65 m (though note that a longer range version of the F5 is also available with a maximum range of 4.5 m). The short exposure time (3 ms) means that the device captures scene geometry in free motion and thus can be mobile around complex scene geometries. Video data are displayed on an attached control unit; however, data processing does not take place until after the survey is complete. Manual movements of the sensor require co-

ordination with the display live-view, and in practice the speed and quality of data collection are influenced by operator experience (Kersten et al., 2016). For this study, high resolution plot surveys were conducted in a matter of seconds. To improve the registration of individual frames (especially on flat relatively featureless surfaces), geometric objects (cuboids, cylinders, etc.) were placed near each plot corner. In addition, despite the low sensitivity to ambient light, the plot was kept in the shade during the final surveys which took place on a bright sunny day.

[FIGURE 4]

Alignment of the HhI point clouds with those derived from SfM-MVS was achieved by manually picking >5 common tie-points in each survey. Since alignment errors are similar to anticipated differences between survey methods, the focus of this study is not of a direct quantitative evaluation of point elevations (e.g. through a DEM of Difference). Instead, the focus of this study is to compare the ability of each method to represent individual features on the peat surface and, crucially, to quantitatively compare roughness metrics calculated from each data set. A 1 mm resolution HhI DEM of each plot was generated, again using the mean elevation within each cell.

3.4 Roughness Analysis

Roughness metrics each provide a particular summary of the topographic variability of a given surface (typically at a 'sub-grid' scale) focusing on a specific aspect of that surface. As such, no single quantity can be defined uniquely as roughness (Smith, 2014) and complex surfaces cannot be described fully by a finite number of parameters (Gadelmawla et al., 2002). In this exploratory analysis, a range of roughness metrics were computed to determine those that best discriminate different peat surface microtopographic types. In this application we use the methodology to distinguish between peat flats, microterraces, wind

ridges and pedestals (Figures 1 and 2). Following the classification of roughness metrics and discussion in Smith (2014), the parameters examined here are divided into six categories (see Table 1):

(1) **Bulk amplitude parameters**: these quantify elevation variance of the points normal to a surface (often described as 'relief') and do not take into account the spatial relationship between each point. Such amplitude parameters are often calculated from the probability distribution of elevation values, by far the most common of which is the standard deviation of elevations σ_z that is seen almost as a 'default' roughness parameter in geomorphological literature (e.g. Sankey et al., 2010; Nield et al., 2011; Brasington et al., 2012). In addition to σ_z, skewness and kurtosis of the probability distribution were calculated (Aberle and Nikora, 2006; Aberle et al., 2010) and, since the topographic data were non-normally distributed (albeit with only minor departures from normal), the inter-quartile range is calculated as a non-parametric alternative.

(2) **Localised elevation differences**: while the above parameters provide a summary over the whole plot (~0.7 m^2), other authors have estimated roughness at a much smaller scale (relative to the DEM extent) and summarised these localised elevation variance values over the whole plot (e.g. Riley et al., 1999; Sankey et al., 2011). Here three scales of local calculation were evaluated. First, using a 50 mm sampling window (identified as the typical dimension of a pedestal or wind ridge) the deviation of each point from a best-fit plane over the sampling window was calculated and the median value across the plot reported. To represent the largest local roughness features in the suite of roughness metrics, the 95th percentile of the plot deviations was also reported. Second, following the tradition of reporting nearest-neighbour elevation differences for DEMs (in this case of 5 mm resolution), the maximum and root-mean squared (RMS) differences between neighbouring grid cells were

computed (the latter of which is termed 'ruggedness' by Riley et al., 1999). Finally, at the finest scale, the mean elevation range within each 5 mm cell was calculated.

(3) **Spacing parameters**: these evaluate the density of features identified on the surface. Using the 5 mm DEM of each plot, peaks and pits were identified through analysis of the elevation of each cell relative to the 8 neighbours and the density of these features within each plot calculated.

(4) **Hybrid parameters**: these combine both elevation variability and spacing aspects and, as such, are typically slope-related terms. Compared with amplitude parameters, hybrid parameters are much more dependent on sample spacing. The mean and standard deviation of all local slopes on the 5 mm DEM were calculated, with the latter found to be a useful measure for morphometric analysis by Grohmann et al. (2011). The statistical variability of the normals of the slopes can be an informative roughness metric; Woodcock (1977) and McKean and Roering (2004) use the orientation tensor method to compute the three normalised eigenvalues (S_1, S_2, S_3) that describe the amount and nature (i.e. uniaxial cluster or girdle) of clustering of vector orientations. The logarithms of two ratios ($\ln(S_1/S_2)$ and $\ln(S_2/S_3)$) are computed. Where S_1 is higher than other eigenvalues, orientation data are clustered (as might be expected of a smooth surface); where both S_1 and S_2 are higher than S_3, a girdle-like pattern is observed (McKean and Roering, 2004). Although these metrics are often computed together for graphical analysis, here they are both individually included in the exploratory search for an objective classification of peat surface roughness types.

So-called 'tortuosity' measures as used commonly in geomorphology (e.g. Morgan et al., 1988; Moser et al., 2007) are also considered as 'hybrid' parameters. These compute the ratio of a measured surface profile length with that of the equivalent

straight line. Here the tortuosity of orthogonal profiles from all rows and columns of the DEM was calculated and the mean value reported. Similarly the frontal area per unit planar area was calculated and averaged across all cardinal directions. As wind erosion is commonly observed on peat surfaces, the aerodynamic roughness height z_0 (a combination of frontal area and amplitude measurements, following the raster-based implementation in Smith et al., 2016) was also estimated for each cardinal direction and the mean value reported.

(5) **Geostatistics and multi-scale parameters:** semivariograms are commonly used to represent the variation of a vertical length scale with increasing lag distance. Semivariograms were calculated for each plot and, where a spherical model provided a good degree of fit (in all but two cases), the fitted range and sill values recorded (Oliver and Webster, 1986). Power spectra were also calculated for each surface; these also represent the way in which roughness or spectral power varies with wavelength. Radially-averaged power spectra decompose the observed topographic variation into different scales (following a two-dimensional Fourier decomposition) and have been shown to exhibit scale invariance such that a power-law equation can be fit between spectral power and wavelength (Turcotte, 1997). The slope of the power spectral density function was calculated following Aberle et al. (2010).

(6) **Anisotropy parameters:** these evaluate the extent to which topographic variability is isotropic and may identify features aligned to prevailing wind or water flow directions, for example. The geostatistical range and sill described above were calculated in directional semivariograms with 22.5 degree windows (as per Vázquez et al., 2005) and the ratio of the minimum and maximum values used to represent the degree of anisotropy (with values approaching unity being isotropic). z_0 and surface frontal area were also calculated for each cardinal direction and the anisotropy of these estimated

in the same way. The anisotropy of tortuosity was also calculated in this manner using just the orthogonal profile values.

[TABLE 1]

In total, 26 roughness metrics were computed for each surface. For a metric to be useful, it must be robust for characterising the feature of interest given the data quality available. Rarely is SfM-MVS evaluated in its ability to represent roughness (Eltner et al., 2016); however, such validation is essential if peat surface types are to be identified from SfM-MVS derived roughness values. Thus, each roughness metric was calculated using both SfM-MVS data and HhI data on the three plots where both data were available (5mm DEMs were used for roughness calculation). Differences between roughness values reflect both the differences between the survey methods (as discussed in a recent methodological comparison by Thomsen et al., 2015) and the robustness of the roughness metric in representing the feature of interest. If a roughness metric is sensitive to methodological differences, then it is of limited use for an objective classification using SfM data. Thus, for inclusion in the objective classification of bare peat surface types, it needs to be demonstrated that the roughness metric is reliable and can discriminate between surface types regardless of survey method. In comparing roughness metrics between surface types and survey methods, there are 4 possible scenarios:

(i) **Identical values for each method:** differences in survey precision have no effect on the value of the roughness metric. The values for each surface type are identical for the different survey methods.

(ii) **Systematic offset:** the SfM model may not be able to recreate the sub-mm details observed in the HhI model so differences between the absolute values of a roughness metric would be expected. However, if the difference between them is systematic (e.g. HhI values consistently higher than SfM values) then it will not influence the objective classification.

(iii) **Offset is bigger than differences between microtopographic types:** the order of microtopographic types may be the same for each survey method, but there is some overlap in the roughness metric values. While not ideal, this would still be acceptable for the objective classification as, crucially, the order is preserved.

(iv) **Metric is non-robust to survey precision:** the lower precision of the SfM data influences the roughness metric in a non-systematic way. Relative to the HhI value, some surfaces exhibit higher roughness values while others exhibit lower roughness values. The order of the surface types is not preserved and thus the surface is not adequately represented by the SfM topographic model when judged on this roughness metric.

For the objective classification described below, scenarios (i) and (ii) are advantageous, though (iii) is also acceptable. Scenario (iv) is not appropriate as the roughness value is dominated by the survey method rather than reflecting the 'true' surface.

3.5 Objective classification of microtopographic surfaces

Decision trees were used to identify and describe structural patterns in the data and identify peat microtopographic type (i.e. an objective variable) in terms of a suite of roughness metrics (i.e. explanatory variables). Decision tree analysis has been used previously in many geomorphological investigations, including landform detection from remotely sensed imagery (e.g. Schneevoigt et al., 2008); landslide susceptibility assessment (e.g. Saito et al., 2009) and to classify land cover (e.g. Pal and Mather, 2003). It is a computationally fast technique that makes no statistical assumptions. The Weka software programme was used to produce a method of classifying the peat surfaces based on the calculated roughness metrics. The J48 top-down recursive 'divide-and-conquer' classification method was used, based on the C4.5 statistical classifier and used to generate a decision tree (Witten et al., 2011). The J48 classifier was used to identify the minimum number of roughness metrics needed to correctly classify peat microtopographic roughness with information theory-based heuristics used to

select each node based on quantification of entropy in terms of 'information gain'. All roughness metrics were normalized prior to analysis. The classification program was run using all the peat surfaces as a training data set to establish the maximum accuracy and produce the best possible decision tree.

While the final decision tree used all surfaces to train the classifier, two tests the decision tree approach were performed, separating the data into training and validation sets. First, 66% of the total data were used as training data and the model then evaluated on the remaining 34% to provide an independent check on the ability of roughness metrics to distinguish between these surface types. As a second test of model performance, a ten-fold cross-validation was performed where instances are split into ten equal sized sets divided into two groups (9 sets for training and 1 set for validation). The performance of the model is computed as the average of ten repetitions with a different set as the training set for each repetition.

4. Results

First, section 4.1 examines the ability of SfM to represent the fine details of the peat surface through comparison of the 1 mm DEMs generated through SfM and the HhI. Section 4.2 then quantitatively tests the ability of SfM to reproduce roughness metrics of peat surfaces, using the HhI data as a reference. Section 4.3 then summarises roughness values for all SfM plots. Finally, an objective classification of bare peat surfaces is presented in section 4.4 using these SfM-derived roughness metrics.

4.1 SfM-MVS Comparison with HhI data

Registration of each of the HhI point clouds with the corresponding SfM-MVS point cloud yielded an RMSE between tie-points of 1.25-1.77 mm (Table 2). These values are similar to the overall cloud-to-cloud (C2C) elevation differences of 1.40-2.95 mm calculated between all points in the clouds (Girardeau-Montaut, 2016). Therefore, absolute differences between point co-ordinates are not analysed further as point precision is more likely to limit the roughness analysis than accuracy. The stated precision of the HhI was also tested by scanning a planar target surface adjacent to a plot. Based on ~26,600 observations, the median absolute deviation from the plane was just 0.197 mm.

[TABLE 2]

To demonstrate clearly the differences between HhI and SfM-MVS topographic data, 1 mm resolution DEMs are presented (without interpolation of missing points; see Figures 5 and 6); however, roughness analysis are conducted at 5 mm more suited to the SfM-MVS data. The 1 mm DEMs below clearly demonstrate the superior precision of the HhI data which is less apparent in the 5 mm DEMs. However, since some roughness metrics use sub-grid scale information, this finer scale is still important and allows identification of the limits of the SfM-MVS method as applied here. At 1 mm DEM resolution, the lower point density of the SfM-MVS surface models is apparent (Figure 5). The largest differences between the two survey methods were observed at either elevation extreme: the HhI presented microtopographic protrusions as being higher and pits as being deeper than the SfM-MVS model. Features are resolved more sharply with the HhI, indicating that some smoothing is taking place in the SfM-MVS workflow.

These differences are clearer when comparing a smaller subsection of each comparison plot as the fine details are more readily apparent (Figure 6). The HhI resolves tiny details of the

surfaces; for example, small fibrous elements lying on the peat flat surface are seen as a sharp peak (2.73 mm wide, 1.45 mm high) in the transect across the HhI data (Figure 6, right panel). From the orthophotograph (left panel) it appears that this feature is just 2.5 mm in width, but is not detectable in the SfM-MVS DEM (left arrow). Given the linear nature of the feature and lack of surrounding peaks, this is unlikely to be an alignment error. The co-incidence of this peak with a feature in the orthophotograph, along with the sub-millimetre plane deviations described above, lends support to the use of the HhI data as a validation dataset, able to reproduce sub-millimetre topographic variability that is smoothed out of SfM-based models.

A similar comparison can be made on the microterrace plot, where elevation profiles cover both a small particle of unfragmented plant material (arrow close to A) and a pronounced bird footprint indented into the otherwise relatively flat peat surface. In both cases, the vertical extent of the feature is greater in the HhI model (wood 3.0 mm high, footprint 10.7 mm deep) than in the SfM model (1.7 mm and 8.7 mm respectively) (Figure 6). Inspection of elevation ranges of each plot confirms that this effect is present throughout the data. Smoothing does appear to have taken place in the SfM-MVS data with the footprint appearing 25% wider in the SfM model; visual inspection of each DEM, particularly the microterrace, confirms the effect with sharper images more clearly resolved in the HhI DEMs.

At the pedestal plot, the HhI had difficulty in representing the full surface microtopography, with large data gaps evident throughout the plot. From Figure 6 it seems that while some of these gaps are located in shadows, others are not and (from comparison with the SfM DEM) cover areas of both high and low elevation. The gaps are most prevalent on surfaces with a normal vector facing towards the top of the plot as displayed in Figures 5 and 6, which suggests that the most likely cause is that an insufficient range of viewpoints were sampled during the field survey.

[FIGURE 5]

[FIGURE 6]

4.2. Comparison of roughness metrics by survey method

Roughness metrics were calculated based on the full plots, like the examples shown in Figure 5. Here we describe the ability of SfM to characterise a roughness metric robustly in a way that is consistent with the more accurate HhI values. Both SfM and HhI data were available for 3 plots covering a range of roughness types; where the ordering of roughness values is consistent between methods, the metric is considered reliable, especially so when there is no overlap between values for different plots. Figure 7 shows each value scaled to represent the proportion of the range between the smallest and largest value (i.e. all smallest values plot at 0, all largest values plot at 1, a value halfway between the two plots at 0.5). Owing to data gaps in the HhI topographic models (Figure 6), some caution is required in the interpretation of the roughness differences, as the reference HhI topographic models do not fully represent the true surface, especially for the pedestal plot. However, the roughness values were calculated on a 5 mm resolution DEM (whereas the DEMs in Figures 5 and 6 are 1 mm resolution) or the octree-resampled point cloud (~ 7 mm resolution), therefore the data gaps are reduced in these DEMs.

In general, the pedestal plot exhibits the highest roughness values and the peat flat plot the lowest, though with a substantial number of exceptions. The HhI values also typically plot higher than the SfM-MVS values, again, suggesting some smoothing in the SfM-MVS workflow. Encouragingly, only four roughness metrics show inconsistent ordering between survey methods: the ratio of the first two eigenvalues, the gradient of the power spectral density function and the anisotropy ratio of both the geostatistical sill and tortuosity.

Over half of roughness metrics (14 out of 26) clearly discriminate between the plot types (scenario (i) or (ii)), suggesting that SfM-MVS surveys can recreate the relevant features of the peat surface for calculation of these roughness metrics. Three geostatistical metrics (sill, range and the anisotropy ratio of the range) all show a good degree of clustering for each plot. Summaries of vertical length scales across the entire plot (aside from skewness) also distinguish each plot, through there is only a small gap between the microterrace and pedestal surfaces. Metrics that focus on the localised elevation variability also distinguish the plot types, though when considered at the sub-5 mm scale, the HhI exhibits greater variability in elevation. This difference highlights the aforementioned greater prominence of peaks and pits in the HhI model. Considering the density of these peaks and pits, all HhI values were higher than all SfM-MVS values across the three plots. Examination of transects in Figure 6 indicates that this is a smoothing effect of SfM-MVS and thus, although the plot ordering is the same for both methods, point/pit density values from SfM-MVS data should be considered unreliable for further roughness analysis as they are sensitive to data quality.

Hybrid parameters appear to distinguish between microtopographic types effectively. Individual normalized eigenvalue ratios could not distinguish the microtopographic types, though when the ratios are used in combination the plots are discriminated, with microterraces appearing the most like a uniaxial girdle (section 4.4). Only three of the roughness metrics summarising the anisotropy of surfaces (frontal area, z_0 and geostatistical range) showed a consistent ordering between plots.

[FIGURE 7]

4.3. Roughness metrics between microtopographic types

Roughness metrics that either are non-robust or exhibit strong correlations with other metrics that measure a similar surface characteristic were excluded from further analysis. Based on the results in Figure 7, the tortuosity anisotropy and gradient of the power spectral density function were excluded from further analysis as they do not robustly characterise the feature of interest. Both eigenvalue ratios are retained as they are best considered in combination (and did distinguish microtopographic types when considered together) and the anisotropy ratio of the geostatistical sill was retained since the overlap in ordering was only very small. Owing to the big difference between absolute values, peak and pit density were also excluded. Standard deviation of elevations was also removed from analysis since elevation data were non-normal (albeit with minor deviations) and it exhibited a strong correlation ($r = 0.99$) with inter-quartile range of elevations. Similarly, all metrics quantifying localised elevation differences were well correlated (all correlations >0.90); only the median deviation from the plane (50 mm kernel) and within-cell (5 mm) elevation range were retained since these had the lowest correlations with the inter-quartile range and covered two different scales. Skewness was excluded as all values were close to zero.

Thus, 17 roughness metrics were retained for exploratory data analysis. These are summarised in Figures 8-11. Figure 8 presents the distribution of those metrics based on elevation variability, noting that each covers a different scale of analysis (~500 mm, 50 mm and 5 mm). The larger scale metrics (IQR and 50 mm deviation from a plane) clearly distinguish the flat microtopographic type from the others. The microterrace plots display larger variability at the plot scale (Figure 8A) than within a 50 mm window (B) or 5 mm cell (C) and can thus be easily distinguished within a bivariate plot space as seen in Figure 8D. Figure 8D summarises the data for (A) and (B) by providing a graphical description of the central part (approximately half) of each dataset and is created by transforming the coordinates of the data into polar coordinates, smoothing on a periodic scale and transforming back (Cleveland and McGill 1984; Cox 2005). Some differences between the pedestal and wind ridge microtopographic types can be seen in Figure 8D since the latter

typically exhibit a higher IQR and lower deviation within a 50 mm window, but substantial overlaps are observed.

[FIGURE 8]

A similar picture is observed for the 7 hybrid roughness parameters retained for analysis (Figure 9). The peat flat microtopographic type is easily distinguished for all metrics, as is the microterrace type for some metrics (Figure 9A, C and D). While small differences between pedestals and wind ridges can be seen (with pedestals showing higher mean slope, tortuosity and frontal area), the overlaps remain substantial. Eigenvalue ratios (Figure 9F) can distinguish peat flats and microterrace (both of which exhibit high degrees of clustering), but cannot distinguish between pedestals and wind ridges

[FIGURE 9]

A summary of geostatistical parameters is presented in Figure 10A-B while fitted spherical semivariogram models for the maximum, mean and minimum parameter values in each plot type are shown in Figure 10C. Both microterrace and wind ridge plots show similar ranges (Figure 10A). Interestingly the sill value of the pedestals is typically smaller than for the wind ridges, while microterraces show the largest range of values.

Anisotropy ratios typically display a wide variability within each microtopographic type (Figure 11). With the anisotropy ratio representing the minimum value of a parameter as a proportion of the maximum value recorded for a given direction (and thus higher values exhibit a higher degree of isotropy), wind ridges generally display more anisotropy than pedestals, possibly because they are wind-aligned. This greater anisotropy is most evident for the frontal area and aerodynamic roughness metrics (Figure 11C-D). The anisotropy of microterraces, that are stepped in one direction, can also be seen.

[FIGURE 10]

[FIGURE 11]

4.4 An objective classification of peat roughness from high resolution topographic data

The patterns in the roughness metrics described in the previous section clearly show distinct but variable relationships to the four peat microtopographies but the optimal combination of metrics required to robustly define these forms has not been objectively determined. Using the 17 roughness metrics described above, a decision tree analysis was performed. Metrics were standardised prior to analysis, though re-running the analysis on non-standardised data yielded no difference in the model performance. Therefore, values reported in Figure 12 are non-standardised for clarity. The J48 classifier identified 5 roughness metrics that were required to classify the peat surfaces: Inter-quartile Range, Median Deviation from Plane (50 mm), Frontal Area Anisotropy Ratio, Profile Tortuosity and the Geostatistical Sill. One roughness metric from each of the 5 categories of roughness metrics outlined in Table 1 is represented in the decision tree (noting that both spacing parameters were excluded above).

The maximum accuracy using all the data as a training set was 98% (i.e. one plot was misclassified). This decision tree is shown in Figure 12 and described below. When this approach was established on 66% of the data and validated on 34%, the success rate was 85%. The ten-fold cross-validation correctly classified 76% of instances, with the majority of misclassified instances (i.e. all but three) arising from a confusion of wind ridges and pedestals.

In the full model (Figure 12), flats were readily distinguished using IQR (100% correctly classified) while wind ridges were identified as having a higher IQR but lower Median Deviation from the Plane (50 mm), as also seen in Figure 8D. However, one microterrace

can be seen as an outlier in Figure 8D and was misclassified as being a wind ridge plot owing to the larger local elevation variability. Of the remaining 29 observations comprising mostly wind ridges and pedestals, these were mostly separated using an anisotropy metric (F_{ani}) with wind ridges exhibiting higher anisotropy (i.e. lower values of F_{ani}) than pedestals. However, this alone was insufficient to separate wind ridges and pedestals, with 4 instances being routed incorrectly (2 of each type). A further layer was sufficient to correctly route these instances as pedestals were observed to have a higher Tortuosity and lower Geostatistical Sill than wind ridges.

[FIGURE 12]

With plots grouped together at different locations across Moss Flats, the effect of location on values of each of the 5 roughness metrics was analysed statistically for each microtopographic type using a Kruskal Wallis test with the location as the independent variable (a Wilcoxon Mann-Whitney test was used for pedestals which were present at only 2 locations). In general, there were no statistically significant differences in roughness values for each microtopographic type other than for wind ridges, which displayed more location-dependant variability than the other microtopographies, with differences in the bulk amplitude parameter (IQR) being significant to $p < 0.01$ (though frontal area anisotropy and tortuosity were stable across locations).

5. Discussion

This research brings together decades of field observations into a coherent conceptual model of peat surface roughness that, in combination with high-resolution topographic survey methods, is shown to usefully discriminate dominant surface process regimes from topographic data alone. We demonstrate that close-range SfM-MVS surveys provide

topographic data of sufficient precision and resolution to enable field application of the conceptual model we present. While more work is required to expand our approach to the other bare peat surfaces depicted in Figure 2, these results establish a clear methodology for integrating much-needed process understanding into morphometric sediment budgets of bare peat and enable testing of a series of hypotheses about peat erosion mechanisms. Moreover, the general approach is of broader interest to geomorphologists beyond peatlands.

Single roughness metrics are often used to summarise sub-grid topographic variability in geomorphology. However, the analysis presented here indicates that different microtopographic surface types can only be identified when multiple roughness metrics are used in combination. Interrogation of morphological data to infer geomorphological processes has a long history; the study presented here is aligned closely with calls to make the best use of the recent developments in high resolution topographic survey (Passalacqua et al., 2015) and attempts to interrogate high-resolution topographic data for this purpose (e.g. the work of McKean and Roering (2004) using multiple roughness metrics to create an objective classification of landslide occurrence).

The decision tree analysis demonstrated that each of the 5 categories of roughness metric included were represented as discriminatory variables. This result emphasises the importance of representing a range of surface properties by considering different types of roughness metric. These roughness metrics yielded consistent values for each microtopographic type across different areas of Moss Flats, with the exception of wind ridges which displayed greater variability, perhaps indicating differential sheltering. However, the anisotropy metric that best discriminated wind ridges from other types was stable across the study area.

Structure-from-Motion photogrammetry is well-placed to provide the high resolution topographic data needed to capture fine-scale roughness signatures in peat and is well-established in geomorphology (James and Robson, 2012; Westoby et al., 2012; Fonstad et al., 2013; Smith et al., 2015). While validation studies have taken place at a range of scales (see summary in Smith and Vericat, 2015), field validation at this small scale is complicated by the absence of clearly superior reference data. Here we describe the first geomorphological application of the F5-SR hand-held imager to provide such reference data. A survey of a planar target suggests that HhI errors are ~0.2 mm; however, data gaps observed in the HhI point clouds (see Figures 5 and 6) indicate that field data acquisition using the HhI is not problem-free.

From comparison of SfM-MVS with HhI topographic data, it is clear that SfM-MVS can generally reproduce millimetre-scale topographic variability (with 3D differences between point clouds comparable with the georeferencing error at ~2 mm). This finding is in-keeping with laboratory-based SfM-MVS evaluations at similar survey ranges (Nouwakpo et al., 2014). However, SfM-MVS workflows do smooth the topography and do not completely represent the prominence of peaks or the depth of surface depressions and the very finest scale variability is not represented (e.g. elements ~ 1 mm tall). This smoothing is most likely introduced during the Multi-View Stereo stage of the SfM-MVS workflow, arising from patch-based MVS algorithms. Most importantly for the application presented herein, comparison with the HhI values indicates that SfM-MVS data are able to use a range of roughness metrics to reliably discriminate between peat microtopographic types (Figure 7). While spacing parameters (e.g. peat and pit density) and some anisotropy parameters (e.g. tortuosity anisotropy) are too sensitive to the sub-mm (or mm-scale) differences between the true surface (approximated by the HhI) and the SfM-derived data, most metrics tested here were sufficiently robust such that the different surface types could be distinguished using SfM at the plot scale.

Peat flats were clearly identifiable through the low amplitude-based roughness values obtained. Microterraces were identifiable through higher overall amplitude of roughness, but a value that is lower when evaluated at smaller spatial scales (50 mm). Distinguishing between pedestals (formed through rain splash processes) and wind ridges (moulding of peat surfaces by high winds) was perhaps the most problematic. Anisotropy ratios were most effective in distinguishing between these two types (Figure 11), as wind ridges exhibited a greater degree of anisotropy, presumably through their alignment to the prevailing wind direction. Wind ridges showed a more uneven distribution of frontal area between each cardinal direction and, interestingly, a more uneven distribution of aerodynamic roughness height, a metric often calculated to relate morphological surface properties to wind velocity profiles. Pedestals also had a lower Geostatistical Sill than wind ridges, suggesting that they have a lower limit of topographic variability at longer lag distances.

This study considered a simple four-fold classification of bare peat microtopography; however, other microtopographic forms exist but were not directly observed in this study, especially seasonal features such as surface desiccation cracking and frost-fluff (so-called nubbins) (Figure 2). Further work is required to expand this approach into other bare peat microtopographic forms within the new conceptual framework, and also to examine the effect of land management practices (e.g. burning, grazing) on surface microtopography. Furthermore, through fine-scale monitoring of these distinctive microtopographic patterns, the persistence of each surface type would be observed. This would yield valuable insight into the legacy of near-surface conditions and the identification of hybrid forms (e.g. frost fluff superimposed on an underlying microterrace) would allow reconstruction of successive near-surface processes regimes.

Using the approach developed here the morphometric framework of bare peat roughness shown in Figure 2 has been quantified using the decision tree analysis for the first time

(Figure 12). This is important because it paves the way for the automated classification of bare peat surfaces into dominant process regimes which will help improve peatland sediment budget studies and inform restoration strategies for bare peat surfaces (determining, for example, whether a surface should be protected from wind or water erosion).

The focus here is necessarily on bare peat; however, where sparse vegetation is present, high resolution topographic data can be classified automatically to identify and remove vegetation (e.g. the multi-dimensionality criterion of CANUPO; Brodu and Lague, 2012). Further analysis of the type demonstrated here, coupled with meteorological (i.e. temperature, rainfall, wind speed and direction) and geomorphological measurements (i.e. runoff, sediment transport) could identify associations of roughness metrics with the extent and magnitude of peat surface processes alongside expanding the objective classification to include other microtopographic types. Where such information is available, collection of high resolution morphometric data would then become an efficient way to monitor and better understand the spatial and temporal variability of geomorphological processes operating in upland peat.

6. Summary

Owing to the unique material properties of peat, detailed analysis of the form of bare peat surfaces provides valuable information about the dominant process that formed that surface. By carefully considering the range of processes that take place on peatlands, pioneering work by early peatland geomorphologists (e.g. Bower, 1959) has been extended to present the first systematic process-form conceptual model of peat microtopographic types. Further work is needed to establish rates of change for the recognised roughness types and the sedimentary processes that sustain the microtopography. The methodology proposed here

is ideally suited to this task as it is easily deployed and can be used to efficiently compile multiple time series of surface change. Utilising new developments in high-resolution survey methods, we use detailed surface roughness metrics to objectively discriminate between these peat microtopographic types. This research presents opportunities and the tools to embed a greater understanding of geomorphological processes into sediment budget studies and peat management; and can be extended to include bare peat surfaces impacted by anthropogenic processes such as peat mining (Tuukkanen et al., 2014), animal trampling (Pellerin et al., 2006) and burning (Maltby et al., 1990).

Acknowledgements

References

Aberle J, Nikora, V. 2006. Statistical properties of armoured gravel bed surfaces. Water Resources Research 42, W11414. DOI:10.1029/2005WR004674

Aberle J, Nikora V, Henning M, Ettmer B, Hentschel B. 2010. Statistical characterization of bed roughness due to bed forms: a field study in the Elbe River at Aken, Germany. Water Resources Research 46, W03521, DOI:10.1029/2008WR007406

Anderson K, Bennie J, Wetherelt A. 2010. Laser scanning of fine scale pattern along a hydrological gradient in a peatland ecosystem. Landscape Ecology 25: 477−492.

Bauer T, Strauss P, Grims M, Kamptner E, Mansberger R, Spiegel H. 2015. Long-term agricultural management effects on surface roughness and consolidation of soils. Soil and Tillage Research 151, 28−38.

Bemis SP, Micklethwaite S, Turner D, James MR, Akciz S, Thiele ST, Bangash HA. 2014. Ground-based and UAV-Based photogrammetry: A multi-scale, high-resolution mapping tool for structural geology and paleoseismology. Journal of Structural Geology 69: 163-178.

Birnie RV. 1993. Erosion rates on bare peat surfaces in Shetland. Scottish Geographical Magazine 109(1): 12-17

Bower MM. 1959. A summary of available evidence and a further investigation of the causes, methods and results of peat erosion in blanket peat. Unpublished MSc thesis. University of London.

Bower MM. 1961. The distribution of erosion in blanket peat bogs in the Pennines. Transactions of The Institute of British Geographers 29: 17-30.

Brasington J, Vericat D, Rychkov I. 2012. Modelling river bed morphology, roughness and surface sedimentology using high resolution terrestrial laser scanning. Water Resources Research 48, W11519, DOI:10.1029/2012WR012223

Brodu N, Lague D. 2012. 3D terrestrial lidar data classification of complex natural scenes using a multi-scale dimensionality criterion: Applications in geomorphology. ISPRS Journal of Photogrammetry and Remote Sensing 68, 121−134.

Campbell DR, Lavoie C, Rochefort L. 2002. Wind erosion and surface stability in abandoned milled peatlands. Canadian Journal of Soil Science: 82, 85–95.

Carrivick JL, Smith MW, Quincey DJ. 2016. Structure from Motion in the Geosciences. Wiley Blackwell: Chichester.

Castillo C, Pérez R, James MR, Quinton JN, Taguas EV, Gómez, JA. 2012. Comparing the accuracy of several field methods for measuring gully erosion. Soil Science Society of America Journal 76: 1319−1332.

Chávez GM, Sarocchi D, Santana EA, Borselli L, Rodríguez-Sedano LA. 2014. Using Kinect to analyze pebble to block-sized clasts in sedimentology. Computers & Geosciences 72: 18−32.

Charman D. 2002. Peatlands and Environmental Change. Wiley, Chichester, 301p.

Cleveland WS, McGill R. 1984. The many faces of a scatterplot. Journal of the American Statistical Association 79: 809−822.

Cox NJ. 2005. Speaking Stata: Smoothing in various directions. The Stata Journal 5: 574−593.

Daanen HA, Ter Haar FB. 2013. 3D whole body scanners revisited. Displays 34: 270−275.

Dietrich JT. 2016. Riverscape mapping with helicopter-based Structure-from-Motion photogrammetry. Geomorphology 252: 144−157.

Dunkerley D. 2002. Volumetric displacement of flow depth by obstacles, and the determination of friction factors in shallow overland flows. Earth Surface Processes and Landforms 75:165-175.

Eltner A, Kaiser A, Castillo C, Rock G, Neugirg F, Abellán A. 2016. Image-based surface reconstruction in geomorphometry–merits, limits and developments. Earth Surface Dynamics 4: 359−389.

Evans M, Lindsay J. 2010. High resolution quantification of gully erosion in upland peatlands at the landscape scale. Earth Surface Processes and Landforms 35: 876−886.

Evans M, Warburton J. 2005. Sediment budget for an eroding peat-moorland catchment in northern England. Earth Surface Processes and Landforms 30: 557−577.

Evans M, Warburton J. 2007. Geomorphology of upland peat: erosion, form and landscape change. Wiley Blackwell: Chichester.

Evans M, Warburton J, Yang J. 2006. Eroding blanket peat catchments: global and local implications of upland organic sediment budgets. Geomorphology 79: 45−57.

Fonstad MA, Dietrich JT, Courville BC, Jensen JL, Carbonneau PE. 2013. Topographic structure from motion: a new development in photogrammetric measurement. Earth Surface Processes and Landforms 38: 421−430.

Foulds SA and Warburton J. 2007. Wind erosion of blanket peat during a short period of surface desiccation (North Pennines, Northern England). Earth Surface Processes and Landforms 32: 481-488.

Francis IS. 1990. Blanket Peat Erosion in a Mid-Wales catchment During two drought years. Earth Surface Processes and Landforms 15: 445-456

Frankl A, Stal C, Abraha A, Nyssen J, Rieke-Zapp D, De Wulf A, Poesen J. 2015. Detailed recording of gully morphology in 3D through image-based modelling. Catena 127: 92−101.

Gadelmawla ES, Koura MM, Maksoud TMA, Elewa IM, Soliman HH. 2002. Roughness parameters. Journal of Materials Processing Technology 123: 133−145.

Gallego-Sala AV, Prentice IC. 2013. Blanket peat biome endangered by climate change. Nature Climate Change 3: 152−155.

Garnett M and Adamson J. 1997. Blanket mire monitoring and research at Moor House National Nature Reserve in Tallis J, Meade R, Hulme P. (Eds.) Blanket mire degradation causes, consequences and challenges. British Ecological Society, Aberdeen 116-117

Girardeau-Montaut D. 2016. CloudCompare - Open Source Project. http://www.danielgm.net/cc/ (accessed 20 December 2016).

Gorham E. 1991. Northern peatlands: role in the carbon cycle and probable responses to climatic warming. Ecological Applications 1: 182−195.

Grayson R, Holden J, Jones RR, Carle JA, Lloyd AR. 2012. Improving particulate carbon loss estimates in eroding peatlands through the use of terrestrial laser scanning. Geomorphology 179: 240−248.

Grohmann CH, Smith MJ, Riccomini C. 2011. Multiscale analysis of topographic surface roughness in the Midland Valley, Scotland. IEEE Transactions on Geoscience and Remote Sensing 49: 1200−1213.

Hämmerle M, Höfle B, Fuchs J, Schröder-Ritzrau A, Vollweiler N, Frank N. 2014. Comparison of kinect and terrestrial LiDAR capturing natural karst Cave 3-D objects. IEEE Geoscience and Remote Sensing Letters: 11: 1896−1900.

Hodge R, Brasington J, Richards K. 2009. In situ characterisation of grain-scale fluvial morphology using terrestrial laser scanning. Earth Surface Processes and Landforms 34: 954–968.

Hulme PD, Blyth AW. 1985. Observations on the erosion of blanket peat in Yell, Shetland. Geografiska Annaler Series A 67: 119-122.

IUCN UK Peatland Programme. 2017. Peatland Code Version 1.1. Available from: www.iucn-uk-peatlandprogramme.org. Date Accessed: 01/08/2017.

James MR, Robson S. 2012. Straightforward reconstruction of 3D surfaces and topography with a camera: accuracy and geoscience application. Journal of Geophysical Research: Earth Surface 117: F03017, doi: 10.1029/2011JF002289.

James MR, Robson S. 2014. Mitigating systematic error in topographic models derived from UAV and ground-based image networks. Earth Surface Processes and Landforms 39: 1413-1420.

James MR, Robson S, d'Oleire-Oltmanns S, Niethammer U. 2017. Optimising UAV topographic surveys processed with structure-from-motion: Ground control quality, quantity and bundle adjustment. Geomorphology, 280: 51-66.

Kaiser A, Neugirg F, Haas F, Schmidt J, Becht M, Schindewolf M. 2015. Determination of hydrological roughness by means of close range remote sensing. Soil 1: 613−620.

Kersten TP, Przybilla HJ, Lindstaedt M, Tschirschwitz F, Misgaiski-Hass M. 2016. Comparative Geometrical Investigations of Hand-Held Scanning Systems. ISPRS-International Archives of the Photogrammetry, Remote Sensing and Spatial Information Sciences XLI-B5, XXIII ISPRS Congress, 12–19 July 2016, Prague, Czech Republic, 507-514.

Lachat E, Macher H, Landes T, Grussenmeyer P. 2015. Assessment and calibration of a RGB-D camera (Kinect v2 Sensor) towards a potential use for close-range 3D modeling. Remote Sensing 7: 13070−13097.

Lettau HH. 1969. Note on aerodynamic roughness parameter estimation on the basis of roughness element description, J. Appl. Meteorol. 8: 828–832.

Lindsay RA. 1995. Bogs: The ecology, classification and conservation of obrotrophic mires. Scottish Natural Heritage, Edinburgh 119p.

Lindsay RA, Riggall J, Burd F. 1985. The use of small-scale surface patterns in the classification of British peatlands. Aquilo Seria Botanica, 21: 69-79.

Luscombe DJ, Anderson K, Gatis N, Wetherelt A, Grand-Clement E, Brazier RE. 2015. What does airborne LiDAR really measure in upland ecosystems? Ecohydrology 8: 584−594.

Mankoff KD, Russo TA. 2013. The Kinect: A low-cost, high-resolution, short-range 3D camera. Earth Surface Processes and Landforms 38: 926−936.

Maltby E, Legg CJ, Proctor MCF. 1990. The ecology of severe moorland fire on the North York Moors: effects of the 1976 fires and subsequent surface and vegetation development. Journal of Ecology: 78, 490–518.

Manley G. 1942. Meteorological observations on Great Dunn Fell, a mountain station in northern England. Quarterly Journal of the Royal Meteorological Society 68: 151-165.

Manley G. 1943. Further climatological averages from the northern Pennines, with a note on topographical effects. Quarterly Journal of the Royal Meteorological Society 69: 251-261.

McKean J, Roering J. 2004. Objective landslide detection and surface morphology mapping using high-resolution airborne laser altimetry. Geomorphology 57: 331−351.

Mercer JJ, Westbrook CJ. 2016. Ultrahigh-resolution mapping of peatland microform using ground-based structure from motion with multiview stereo. Journal of Geophysical Research: Biogeosciences 121. doi:10.1002/2016JG003478

Moreels P, Perona P. 2007. Evaluation of features detectors and descriptors based on 3d objects. International Journal of Computer Vision 73: 263-284.

Morgan RPC, Quinton JN, Smith RE, Govers G, Poesen JWA, Auerswald K, Chisci G, Torri D, Styczen ME. 1998. The European soil erosion model (EUROSEM): a dynamic approach for predicting sediment transport from fields and small catchments. Earth Surface Processes and Landforms 23: 527−544.

Moser K, Ahn C, Noe G. 2007. Characterization of microtopography and its influence on vegetation patterns in created wetlands. Wetlands 27: 1081−1097.

Nicholson LI. 2016. 3-D surface properties of glacier penitentes over an ablation season, measured using a Microsoft Xbox Kinect. The Cryosphere 10: 1897−1913.

Nield JM, Wiggs GFS, Squirrell RS. 2011. Aeolian sand strip mobility and protodune development on a drying beach: examining surface moisture and surface roughness patterns measured by terrestrial laser scanning. Earth Surface Processes and Landforms 36: 513−522.

Nouwakpo SK, James MR, Weltz MA, Huang CH, Chagas I, Lima L. 2014. Evaluation of structure from motion for soil microtopography measurement. The Photogrammetric Record 29: 297−316.

Oliver M, Webster R. 1986. Semi-variograms for modelling the spatial pattern of landform and soil properties. Earth Surface Processes and Landforms 11: 491−504.

OR3D. 2015. Mantis Vision's F5 Short-Range 3D Imager: technical specifications. www.OR3D.co.uk (accessed 21 December 2016).

Ouédraogo MM. Degré A. Debouche C, Lisein J. 2014. The evaluation of unmanned aerial system-based photogrammetry and terrestrial laser scanning to generate DEMs of agricultural watersheds. Geomorphology 214: 339−355.

Pal M, Mather PM. 2003. An assessment of the effectiveness of decision tree methods for land cover classification. Remote Sensing of Environment 86: 554−565.

Passalacqua P, Belmont P, Staley DM, Simley JD, Arrowsmith JR, Bode CA, Crosby C, DeLong SB, Glenn NF, Kelly SA, Lague D., 2015. Analyzing high resolution topography for advancing the understanding of mass and energy transfer through landscapes: a review. Earth-Science Reviews 148: 174−193.

Pearsall WH. 1956. Two blanket bogs in Sutherland. Journal of Ecology 44: 493-516.

Pellerin S, Huot J, Côté SD. 2006. Long term effects of deer browsing and trampling on the vegetation of peatlands. Biological Conservation: 128, 316-326.

Radforth NW. 1969. Classification of Muskeg (Chapter 2). In Muskeg Engineering handbook, (Ed.) MacFarlane IC, University of Toronto Press, Canada, 31-52.

Riley SJ, DeGloria SD, Elliot R. 1999. A terrain ruggedness index that quantifies topographic heterogeneity. Intermountain Journal of Sciences 5: 23–27.

Repo ME, Susiluoto S, Lind SE, Jokinen S, Elsakov V, Biasi C, Virtanen T, Martikainen PJ. 2009. Large N2O emissions from cryoturbated peat soil in tundra. Nature Geoscience: 2:189–192.

Saito H, Nakayama D, Matsuyama H, 2009. Comparison of landslide susceptibility based on a decision-tree model and actual landslide occurrence: the Akaishi Mountains, Japan. Geomorphology 109: 108−121.

Sankey JB, Glenn NF, Germino MJ, Gironella AIN, Thackray GD. 2010. Relationships of aeolian erosion and deposition with LiDAR-derived landscape surface roughness following wildfire. Geomorphology 119: 135–145.

Sankey JB, Eitel JUH, Glenn NF, Germino MJ, Vierling LA. 2011. Quantifying relationships of burning, roughness, and potential dust emission with laser altimetry of soil surfaces at submeter scales. Geomorphology 135: 181–190.

Schneevoigt NJ, van der Linden S, Thamm HP, Schrott L. 2008. Detecting Alpine landforms from remotely sensed imagery. A pilot study in the Bavarian Alps. Geomorphology 93: 104−119.

Smith MW. 2014. Roughness in the Earth Sciences. Earth Science Reviews 136: 202–225.

Smith MW, Vericat D. 2015. From experimental plots to experimental landscapes: topography, erosion and deposition in sub-humid badlands from Structure-from-Motion photogrammetry. Earth Surface Processes & Landforms 40: 1656−1671.

Smith MW, Carrivick JL, Quincey DJ. 2015. Structure from Motion Photogrammetry in Physical Geography. Progress in Physical Geography 40: 247−275.

Smith MW, Quincey DJ, Dixon T, Bingham RG, Carrivick JL, Irvine-Fynn TD, Rippin DM. 2016. Aerodynamic roughness of glacial ice surfaces derived from high resolution topographic data. Journal of Geophysical Research: Earth Surface 121: 748−766.

Smithson PA. 1985. The Present climate of the Northern Pennines. In Boardman J. (Ed.) Field Guide to the Periglacial Landforms of Northern England. Quaternary Research Association, Cambridge, 1-3.

Tallis JH, Meade R, Hulme PD. 1997. Blanket mire degradation: causes consequences and challenges. Proc. Mires Res. Group. Aberdeen: Macaulay Land Use Res. Inst.

Thomsen LM, Baartman JEM, Barneveld RJ, Starkloff T, Stolte J. 2015. Soil surface roughness: comparing old and new measuring methods and application in a soil erosion model. Soil 1: 399−410.

Tortini R, Bonali FL, Corazzato C, Carn SA, Tibaldi A. 2014. An innovative application of the Kinect in Earth sciences: quantifying deformation in analogue modelling of volcanoes. Terra Nova 26: 273−281.

Turcotte DL. 1997. Fractals and chaos in geology and geophysics. Cambridge University Press: Cambridge.

Tuukkanen T, Marttila H, Kløve B. 2014. Effect of soil properties on peat erosion and suspended sediment delivery in drained peatlands. Water Resources Research: 50, 3523-3535.

Vázquez EV, Miranda JGV, González AP. 2005. Characterizing anisotropy and heterogeneity of soil surface microtopography using fractal models. Ecological Modelling 182: 337−353.

Warburton J. 2003. Wind-splash erosion of bare peat on UK upland moorlands. Catena 52: 191−207.

Washburn AL. 1979. Geocryology: a survey of periglacial processes and environments. Edward Arnold, London, 93-95.

Westoby MJ, Brasington J, Glasser NF, Hambrey MJ, Reynolds JM. 2012. 'Structure-from-Motion' photogrammetry: a low-cost, effective tool for geoscience applications. Geomorphology 179: 300−314.

Williams R. 2012. Section 2.3.2: DEMs of difference. In: Cook SJ, Clarke LE, Nield JM. (Eds.) Geomorphological Techniques (Online Edition). British Society for Geomorphology; London, UK. ISSN: 2047−0371.

Witten IH, Frank E, Hall MA. 2011. Data Mining: Practical Machine Learning Tools and Techniques. (3rd Ed.) Morgan Kaufmann: Burlington USA.

Woodcock NH. 1977. Specification of fabric shapes using an eigenvalue method. Geological Society of America Bulletin 88: 1231−1236.
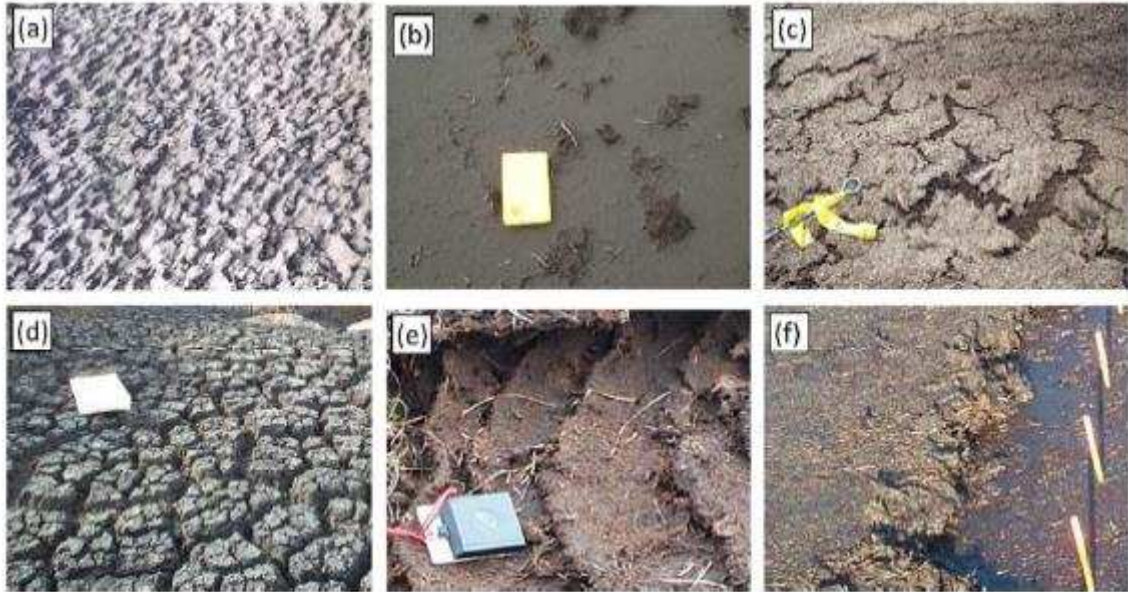
Figure 1. Characteristic surface topography related to dominant process regimes: (a) rainfall – 'toothed' peat pedestals; (b) surface wash – smooth surface infilling of surface irregularities; (c) wind action – surface drying and crusting; (d) surface temperature driven drying and desiccation; (e) wind-ridges – wind-driven rain; and (f) microterrace – wind-driven rain and surface wash. Scale in (a) is approximately 0.5 m long axis of photography. Scales in (b), (c), (d), (e) and (f) shown by notebook (0.15 m long axis), compass (long axis 0.12 m), survey pin (length 0.25 m) and wooden dowels (length 0.12 m).
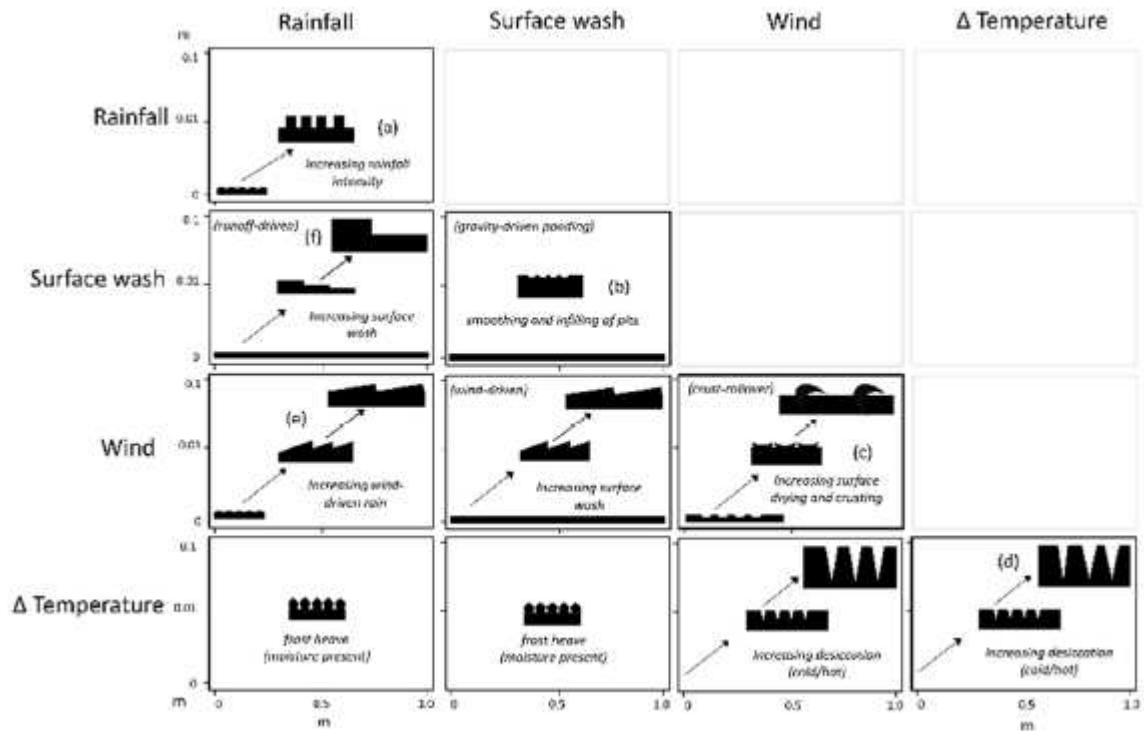
Figure 2. Framework describing process-form relationships for bare peat surface roughness. Each panel shows a schematic of the typical two dimensional (cross-section) form and scale of the surface roughness (length scale 1 m, vertical scale of 0.1 m). Examples of surface roughness types associated with the four panels of the leading diagonal are also shown in Figure 1 (a-d) together with examples of (e) wind-ridges and (f) microterraces.
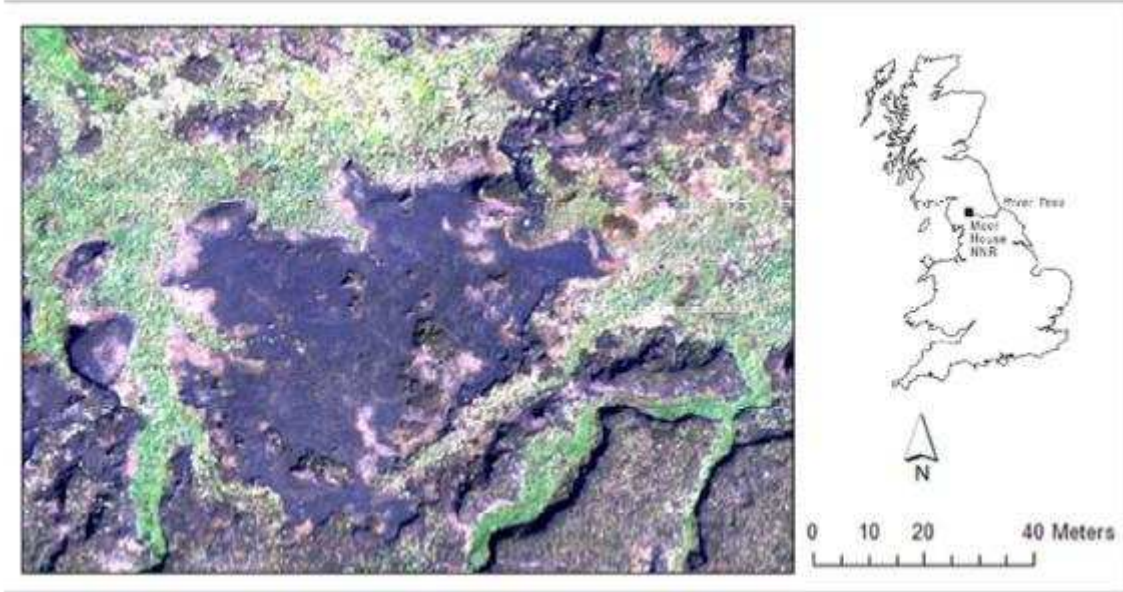
Figure 3. Moss Flats study site, Moor House and Upper Teesdale National Nature Reserve (NNR), North Pennines, Cumbria, UK. Aerial Photograph reproduced under the Open Government Licence v3.0 (OS Open Data).

Figure 4. (A) The Mantis Vision F5 Short Range Hand-held Imager (OR3D, 2015); (B) Use of the HhI on a bare peat plot.
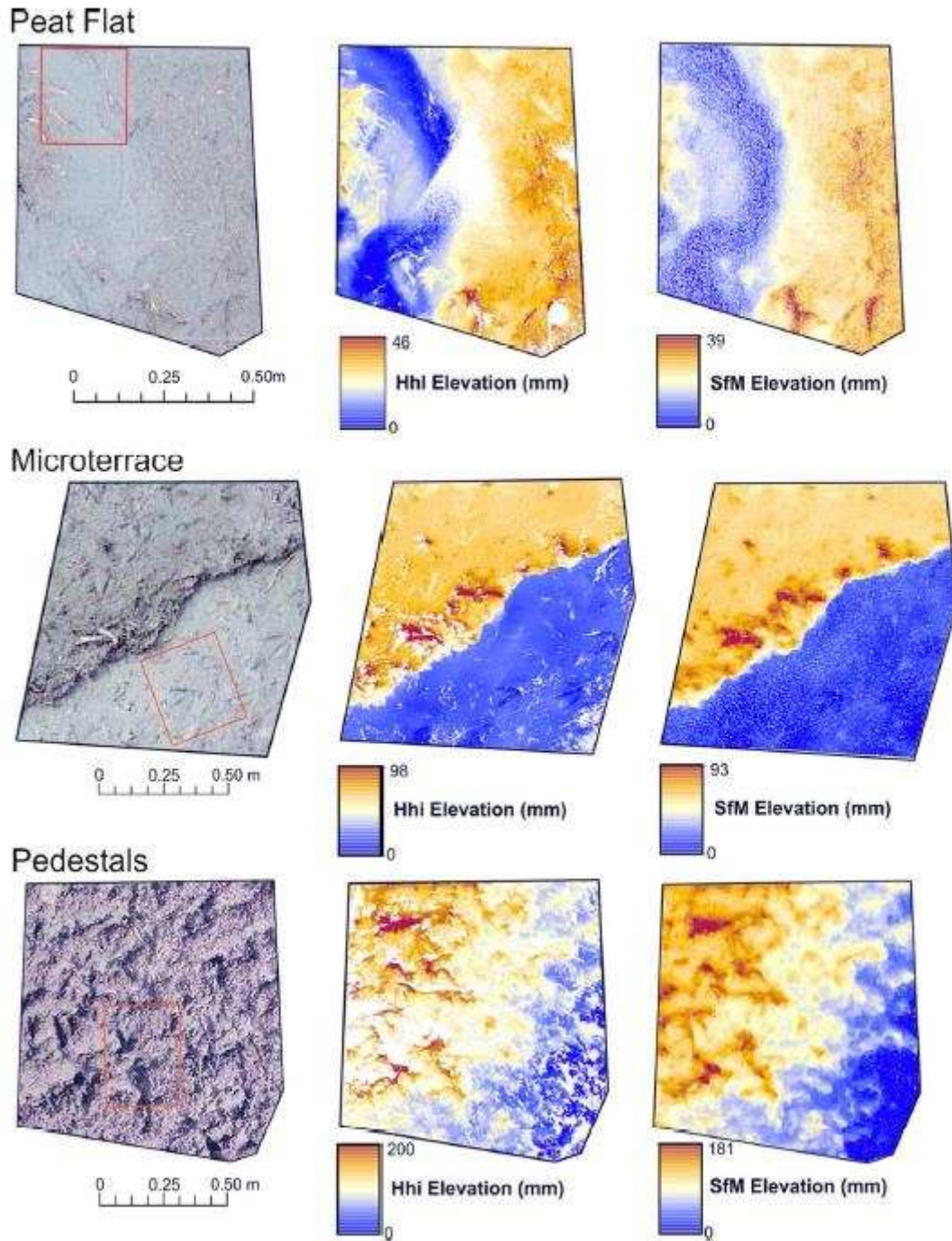
Figure 5. Digital Elevation Models (1 mm resolution) of the three comparison plots. Red boxes on the orthophotographs (left) indicate the zoomed area of Figure 6. HhI DEMs are shown (middle) alongside SfM-MVS DEMs (right) for each plot. The minimum elevation of each survey has been set to zero, to indicate the variable height ranges.
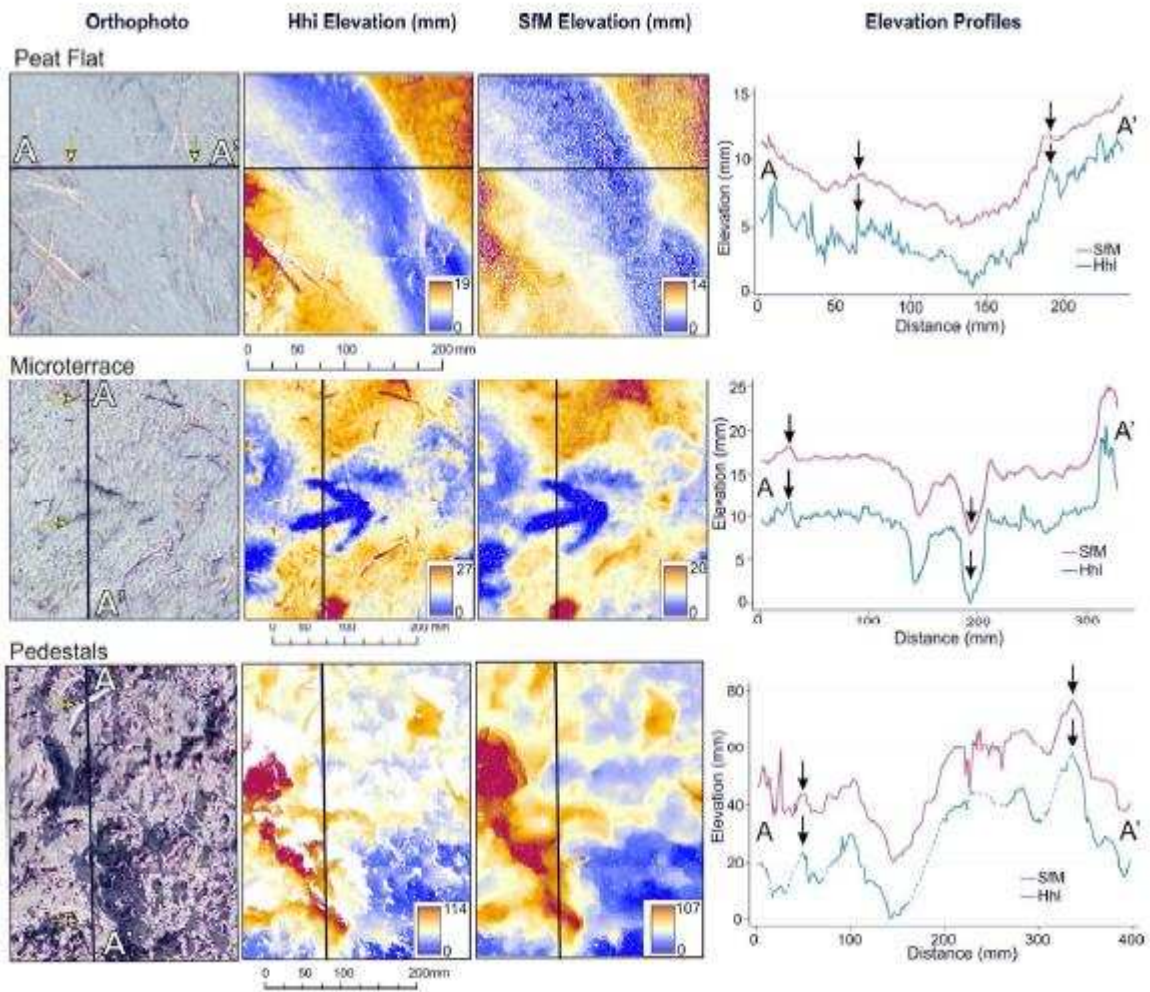
Figure 6. Comparison of HhI and SfM DEMs for a smaller area of interest within the broader plots (Figure 5). Topographic profiles have been taken as indicated and are presented on the right. SfM-derived profiles have been vertically offset to aid visual interpretation. Arrows indicate features evident in the orthophotograph. Dashed lines in the bottom panel indicate interpolation through data gaps.
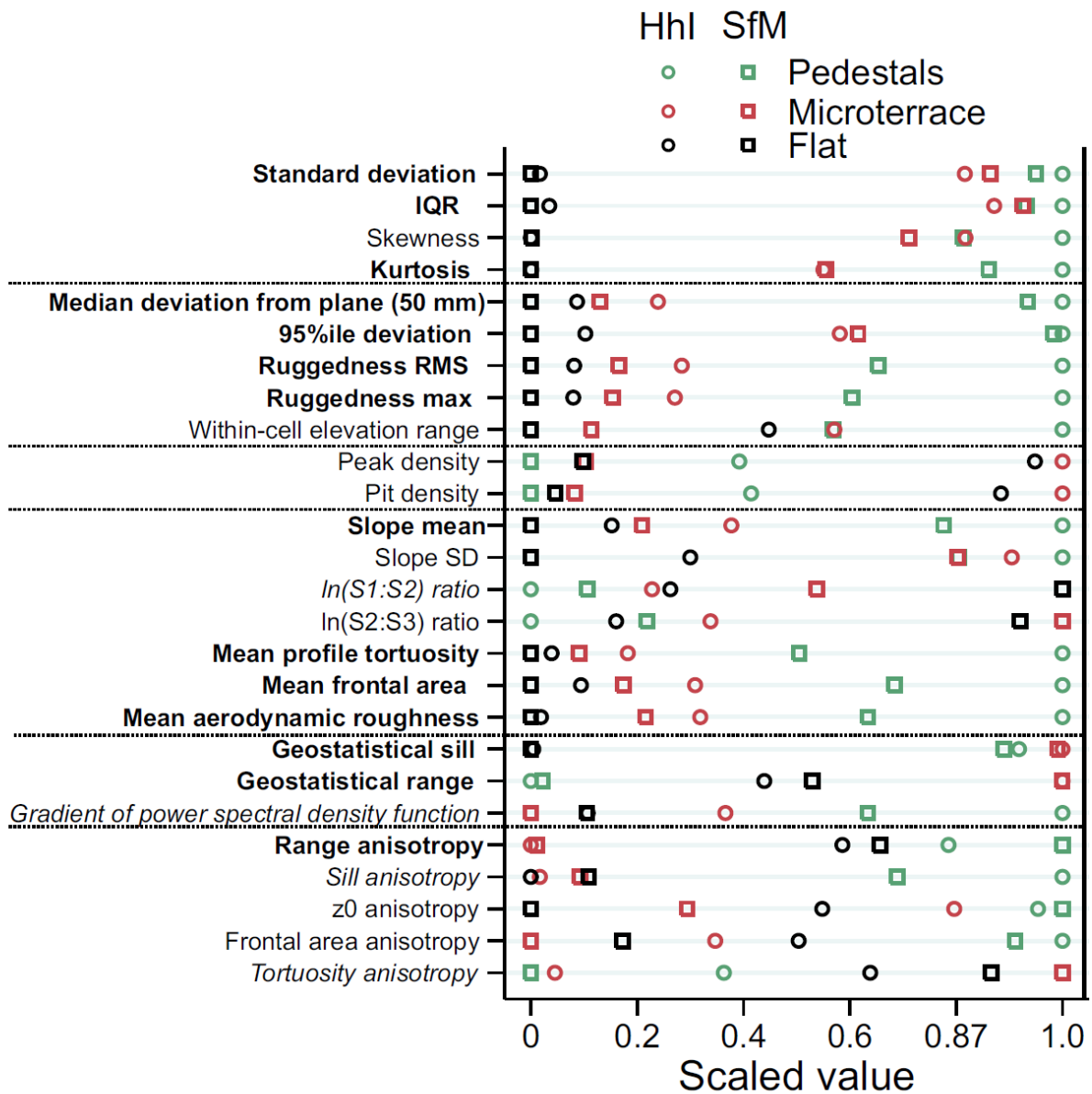
Figure 7. Comparison of roughness values between survey methods and microtopography types. Roughness values have been scaled to represent the proportion of the range between the smallest and largest value (i.e. all smallest values plot at 0, all largest values plot at 1). Roughness metrics in italics show inconsistent plot ordering between survey methods (scenario (iv)) whereas metrics in bold are consistent between survey methods and show no overlap between values for different plot types (scenarios (i) and (ii)).
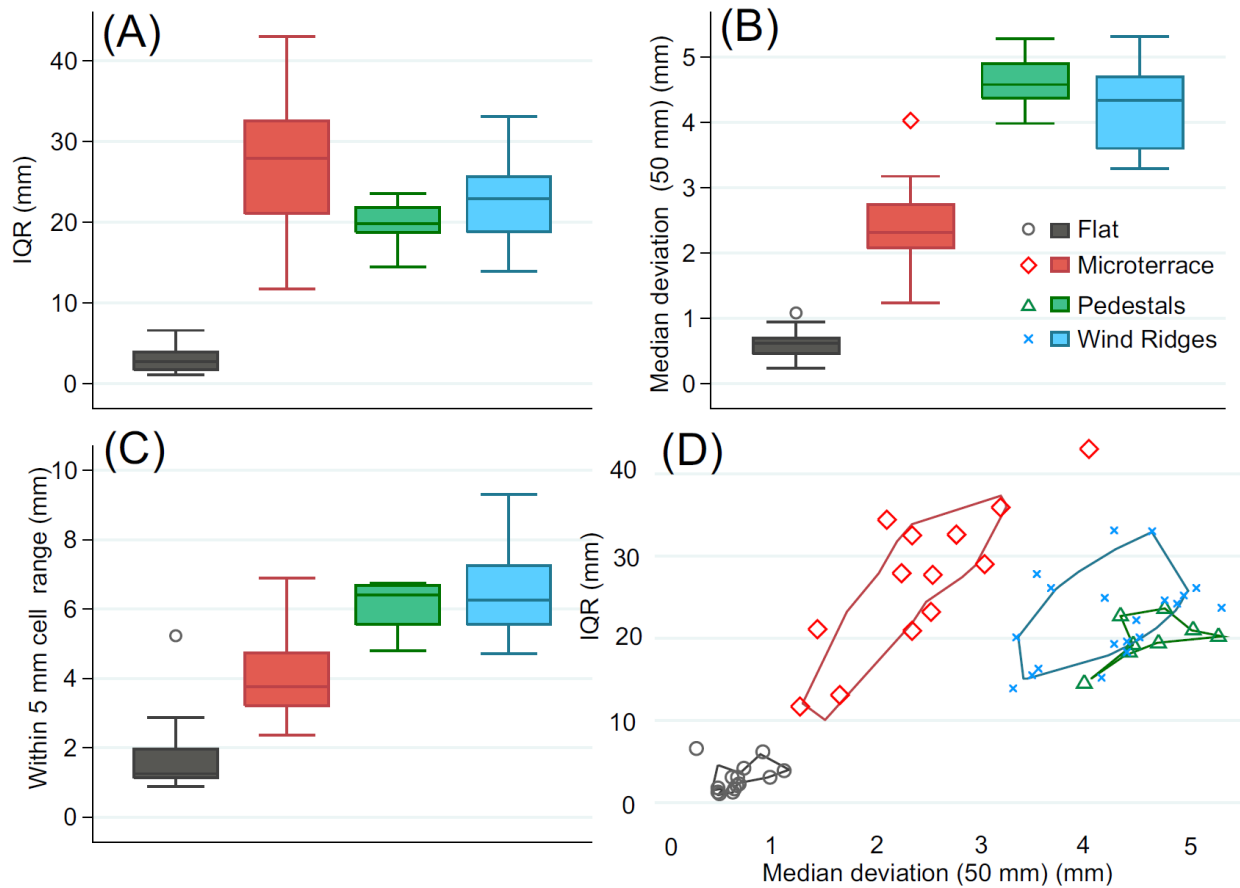
Figure 8. Summary of roughness parameters based on elevation variability (types 1 and 2 in Table 1) evaluated to distinguish between microtopographic types. Variability of (A) IQR (mm); (B) Median deviation from a plane fitted over a 50 mm window (mm); (C) Mean elevation range within 5 mm cells (mm); and (D) polar smooths of IQR against Median deviation over a 50 mm window. Boxes in this and subsequent figures show upper quartiles, medians and lower quartiles; whiskers extend to cover all points within 1.5 times the interquartile range of the quartiles; other points are shown separately.
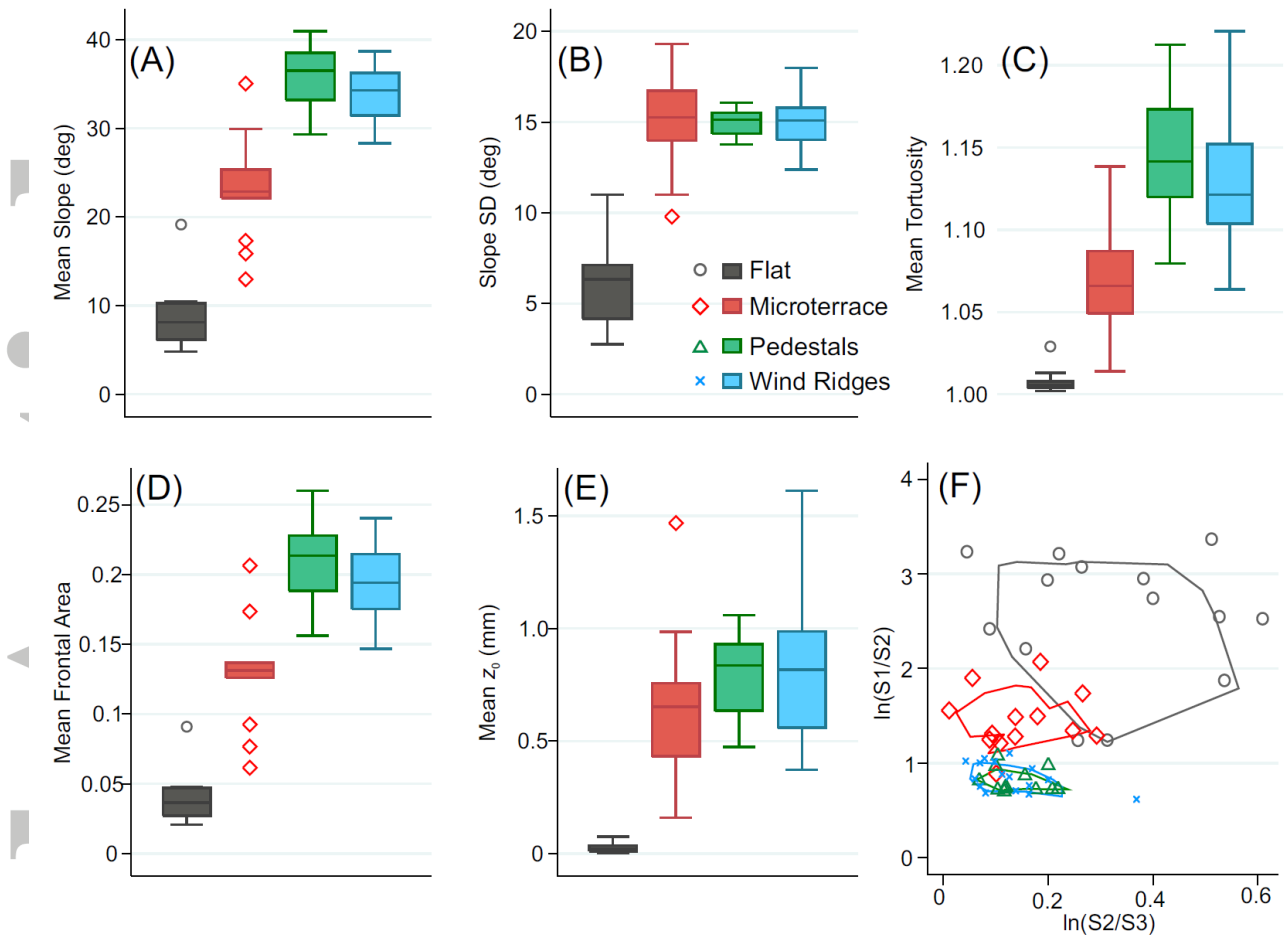
Figure 9. Summary of retained hybrid roughness parameters by microtopographic type: (A) Mean slope (degrees); (B) Slope Standard Deviation (degrees); (C) Mean tortuosity; (D) Mean frontal area; (E) Mean aerodynamic roughness; (F) polar smooths of normalised eigenvalue ratios.
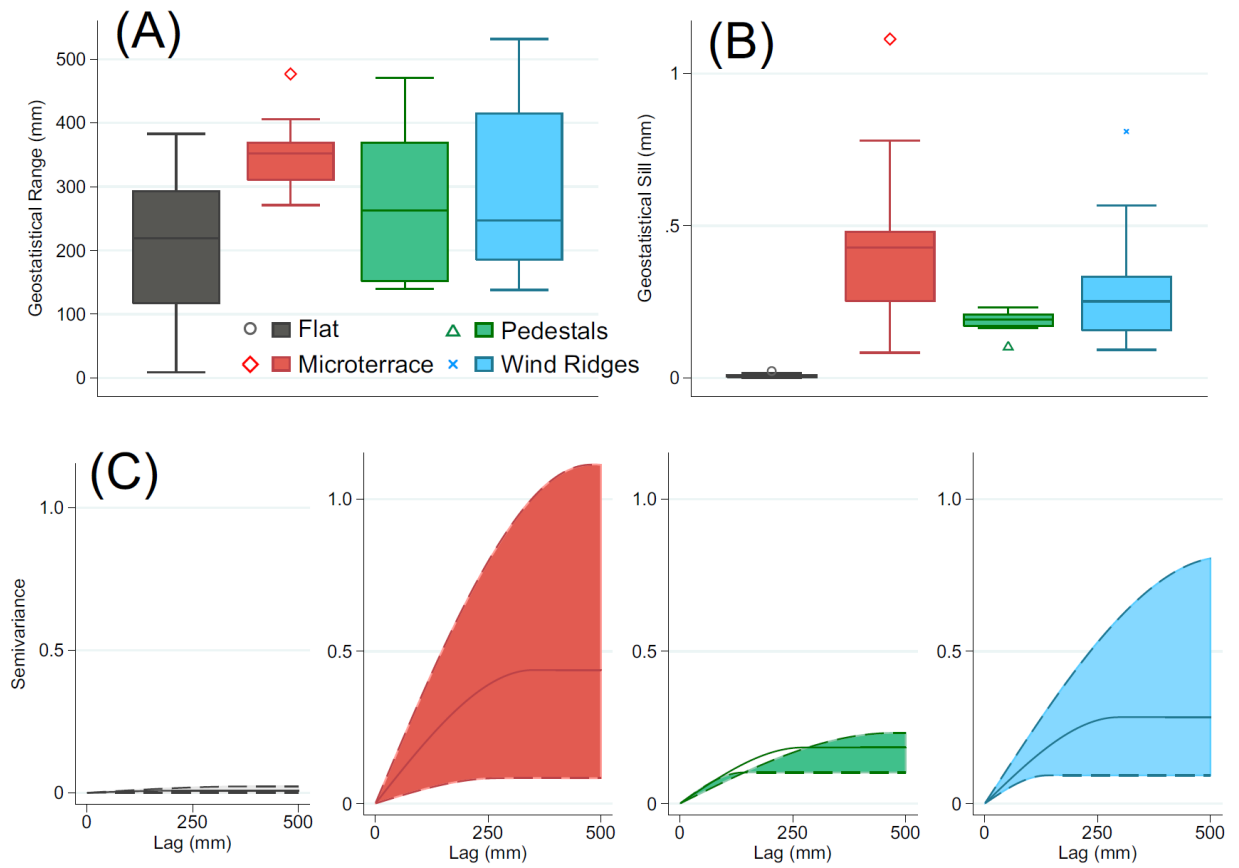
Figure 10. Summary of geostistical parameters by microtopographic type: (A) Range (mm); (B) Sill (mm). (C) fitted spherical semivariogram models for the maximum (dash), mean (solid line) and minimum (dash) parameter values in each plot type.
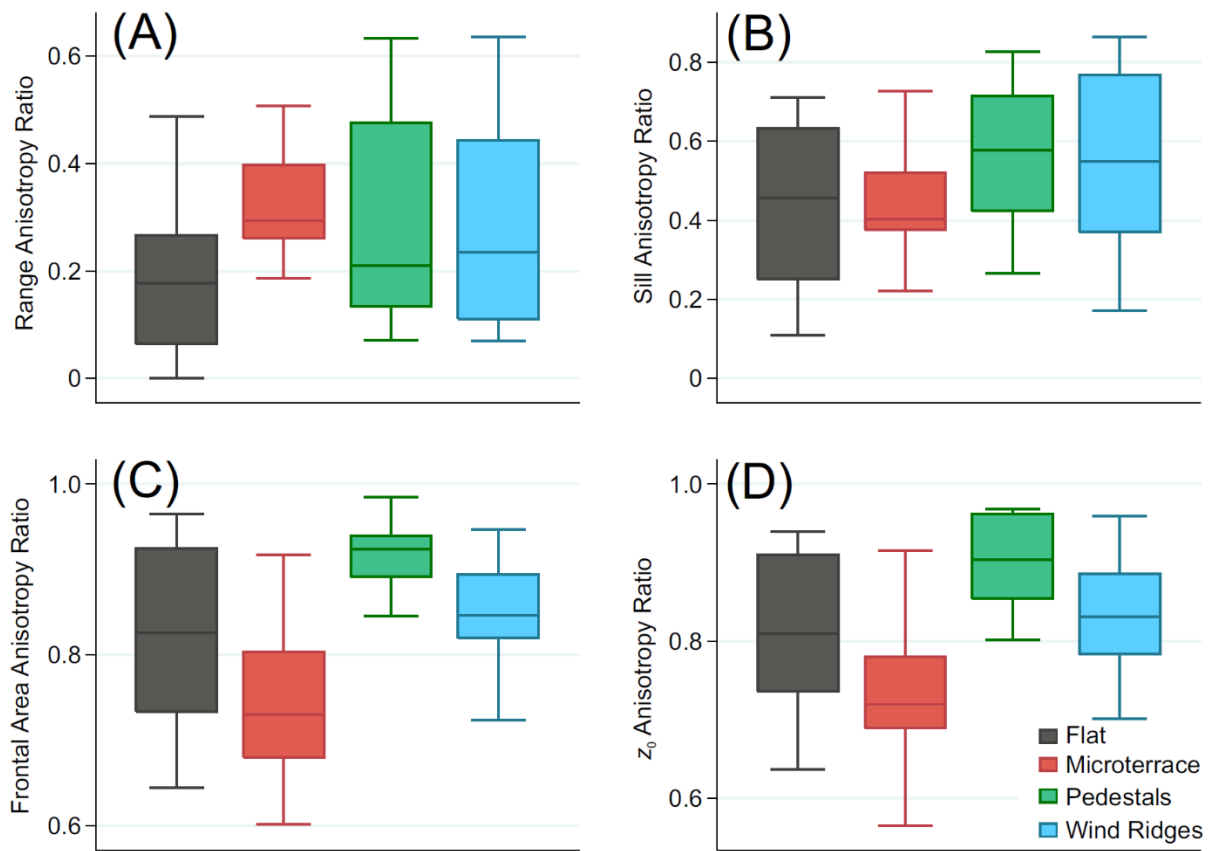
Figure 11. Summary of anisotropy ratios by microtopographic type: (A) Range; (B) Sill; (C) Frontal Area per unit planar area; (D) aerodynamic roughness.
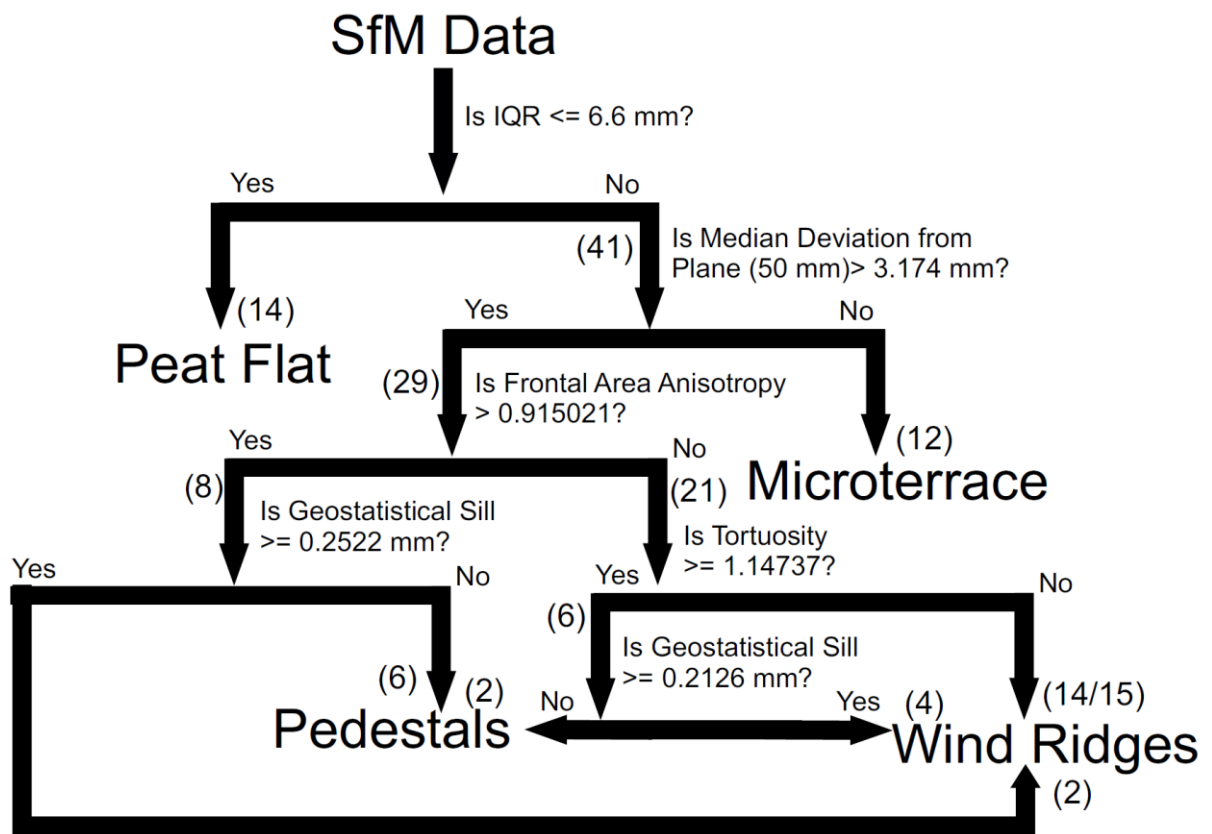
Figure 12. Decision tree for peat surfaces based on roughness metrics. Numbers in parentheses represent the number of instances routed along each path. For wind ridges, the number of correctly routed instances is shown followed by the total number routed along that path.

Tables

Table 1. Overview of roughness metrics calculated for each plot. Plots were linearly detrended prior to roughness analysis. Metrics in bold were used in the decision tree analysis.

Roughness Metric	Notation	Units	Description	Data
[1] Bulk Amplitude Parameters (Elevation Probability Distribution-Based)				
Standard deviation of elevations	σ_z	m	Standard deviation of elevations over the whole plot	Cloud
Inter-quartile range	IQR	m	Inter-quartile range of elevations over the whole plot	Cloud
Skewness	Z_{sk}	-	Skewness of above elevation distribution	Cloud
Kurtosis	Z_k	-	Kurtosis of above elevation distribution	Cloud
[2] Localised Elevation Differences				
Median deviation from plane (50 mm window)	Z_{50-50}	m	Median point deviation from a fitted plane (50 mm kernel size)	Cloud
95th %ile deviation from plane (50 mm window)	Z_{50-95}	m	As above, but the 95th percentile to highlight the roughest areas	Cloud
Ruggedness RMS	Rug_{RMS}	m	Root-Mean-Squared (RMS) of nearest neighbour elevation differences	DEM
Ruggedness max	Rug_{MAX}	m	Maximum of nearest neighbour elevation differences	DEM
Within-cell elevation range	Z_{R-5}	m	Mean of height ranges within each 5 mm cell	DEM
[3] Spacing Parameters				
Peak density	Pk	m^{-2}	Density of peaks	DEM
Pit density	Pt	m^{-2}	Density of pits	DEM
[4] Hybrid Parameters				
Mean slope	S_m	°	Mean of cell slopes	DEM
Standard deviation of slopes	S_σ	°	Standard deviation of cell slopes	DEM
Ratio of 1st and 2nd eigenvalues	$\ln(S_1/S_2)$	-	Normalised eigenvalue ratios of directional data calculated from the orientation tensor	Cloud
Ratio of 2nd and 3rd eigenvalues	$\ln(S_2/S_3)$	-	As above	Cloud
Profile tortuosity	T	-	Ratio between surface profile and straight line length, averaged over each row and column of the DEM	DEM
Frontal area (per unit planar area)	F	-	Roughness element frontal area per unit ground area, averaged for each cardinal direction	DEM
Aerodynamic roughness	z_0	mm	Following Lettau (1969) and Smith et al. (2016). Calculated as the mean height of points above a detrended plane multiplied by a drag coefficient (0.5) and the ratio between the frontal area (above the detrended plane) and full plot planar area	DEM
[5] Geostatistics and Multi-Scale Parameters				
Geostatistical range	a	m	Range of fitted semivariograms	Cloud
Sill	c	mm	Sill of fitted semivariograms	Cloud
Slope of power spectral density function	PSD	-	Slope of the power law relationship between radially-averaged spectral power and wavevectors	DEM
[6] Anisotropy Parameters				
Range anisotropy ratio	a_{ani}	-	Anisotropy ratio (i.e. minimum:maximum) of the ranges of directional semivariograms calculated in 22.5 degree windows	Cloud
Sill anisotropy ratio	c_{ani}	-	As above for the sill of fitted semivariograms	Cloud
z_0 anisotropy ratio	Z_{0ani}	-	Anisotropy ratio of z_0 calculated for all cardinal directions	DEM
Frontal area anisotropy ratio	F_{ani}	-	Anisotropy ratio of frontal area calculated for all cardinal directions	DEM
Tortuosity anisotropy ratio	T_{ani}	-	Anisotropy ratio of tortuosity calculated on perpendicular transects	DEM

Table 2. Differences between HhI and SfM surveys. Point density is calculated prior to octree subsampling.

Plot	Tie point RMSE (mm)	Mean C2C Elevation Difference (mm)	Point Density (HhI) (points mm^{-2})	Point Density (SfM) (points mm^{-2})
Flat	1.252	1.404	4.744	1.087
Microterrace	1.486	2.954	7.520	2.353
Pedestals	1.766	1.162	4.742	3.388

Microtopography of bare peat: a conceptual model and objective classification from high-resolution topographic survey data

Smith, M.W.* and Warburton, J.

- Detailed analysis of the form of bare peat surfaces provides valuable information about the dominant process that formed that surface.

- We outline a new conceptual framework of peat surface roughness types by relating observed forms to the dominant processes responsible for their formation.

- Peat microtopographic types can be identified objectively from high resolution survey data.